Scanning Transmission Electron Microscopy of HSLA Steels

by

J.D. Embury

&

G.C. Weatherly

Annual Report

on

Research Contract

for

Department of Energy, Mines and Resources

"Scanning Transmission Electron Microscopy of High Strength Low Alloy Steels"

Submitted to

Dr. J.D. Boyd

&

Dr. T. Malis

by

J.D. Embury

&

G.C. Weatherly

October, 1982

Scanning Transmission Electron Microscopy of High Strength Low Alloy Steels

Introduction

The overall objective of the current work is to demonstrate the applicability of the scanning transmission electron microscopy (STEM) technique to the study of the evolution of the microstructure of HSLA steels and their modification by welding.

An important feature of this study has been to simulate the initial cooling operation in order to determine both the influence of the initial cooling rate and the evolution of the final microstructure from the dendrite structure. In the past six months considerable effort has been devoted to the study of the as cast structure including the development of new metallographic methods of revealing the evolution of the final structure. This has of necessity involved experimental effort in the area of optical metallography and extraction replica techniques as well as STEM studies.

The influence of cooling rate on the Ti/Nb ratio of the various carbo-nitride phases has been studied in order to attempt to ascertain the initial solidification path at high cooling rates. In addition the Ti/Nb ratio of the carbo-nitrides has been determined for various isothermal reheat cycles. The approach is of importance both in relation to existing models of the precipitation sequence and in order to determine the availability of the microalloy elements for precipitation reactions in subsequent parts

of the total thermo-mechanical history.

To date the STEM techniques have been well developed for the quantitative determination of the ratios of the microalloying elements present in precipitates. However, to date it has proved extremely difficult to obtain equivalent data concerning the ratio of the non-metallic elements. Prior to the development of a reliable system of analysis of the carbon nitrogen ratio in unknown phases it is necessary to develop a system of basic standards for transition metal carbo-nitrides of uniform thickness. In the past three months some effort has been devoted to the preparation of standards and these initial attempts are outlined in a later section of the report.

For clarity the results dealing with the various topics outlined above are reported in separate sections in the results section. However, two other sections are also included in the report. An introductory section due to Dr. S.V. Subramanian outlines the relationship between the present work and the thermal history of various points in a continuously cast ingot. In addition this section outlines the basic problem of deducing the solidification path and temperature range of initial precipitation from the measured Ti/Nb ratios. However, it must be emphasized that in order to quantify this work in a useful manner in the future it is necessary to deal with materials of carefully controlled nitrogen content and in some instances more rapid solidification rates. The final section is in the form of a paper to be published by the Institute of Metals, U.K. based on the work reported

in the present study. The paper concerns "The Microchemistry of Carbonitrides in the Heat Affected Zone of HSLA Steels". This paper gives a comprehensive view of the work to date on the characterization of precipitates after various thermo-mechanical sequences.

Industrial Significance of High Solidification Rate Studies

(this section relates to recent work by Dr. S.V. Subramanian)

In order to model the heat flow process in continuous casting and its influence on important problems such as the occurrence of surface cracking it is essential to consider the cooling process at various points on the cast slab. This has been done and the cooling process computed for three points in a slab 188 cm wide and 20 cm thick. In relation to the total width and thickness the points selected were A at (0.5 cm, 0.5 cm); B at (94 cm, 0.5 cm) and C at (94 cm, 10cm), i.e. C is at the geometric centre of the slab. For all the computations the slab velocity was assumed to be 2.16 cm/sec. The forms of the cooling curve for the various points are shown in figure 1 and 2. The salient features of this simulation are a) that the total time of freezing varies from 3 secs at A to 6.5 secs at B up to 982 secs at C. In addition, the initial cooling rate varies from 110 K/sec for A down to 0.219 K/sec at C.

Given the solidification data and the measurements of Ti/Nb ratios the objective is to try and calculate the solidification path. This can be accomplished by considering the effective values of the distribution coefficient between liquid and delta ferrite or liquid and austenite for the various microalloy elements. This type of calculation is not yet complete and thus is not reported in detail. However, the initial calculation indicates the following tentative conclusions.

a) The solidification path appears to occur through delta ferrite

b) In slow cooled samples precipitation ocuurs at higher temperatures (well above 1500 K)

c) In fast cooled samples precipitation may occur around 1500 K.

Clearly a great deal more work is needed to relate the current STEM data to the models of continuous casting. However, a number of important points emerge in regard to future work. For example the high cooling rates (110 K/sec) at point A indicate that the range of cooling conditions must be extended. Further the measurement of Ti/Nb ratios must be performed in cases where the chemistry is well characterized in terms of C and N also. Finally it is appropriate in the future to study continuously cast slabs directly, in addition to the laboratory samples used to date.

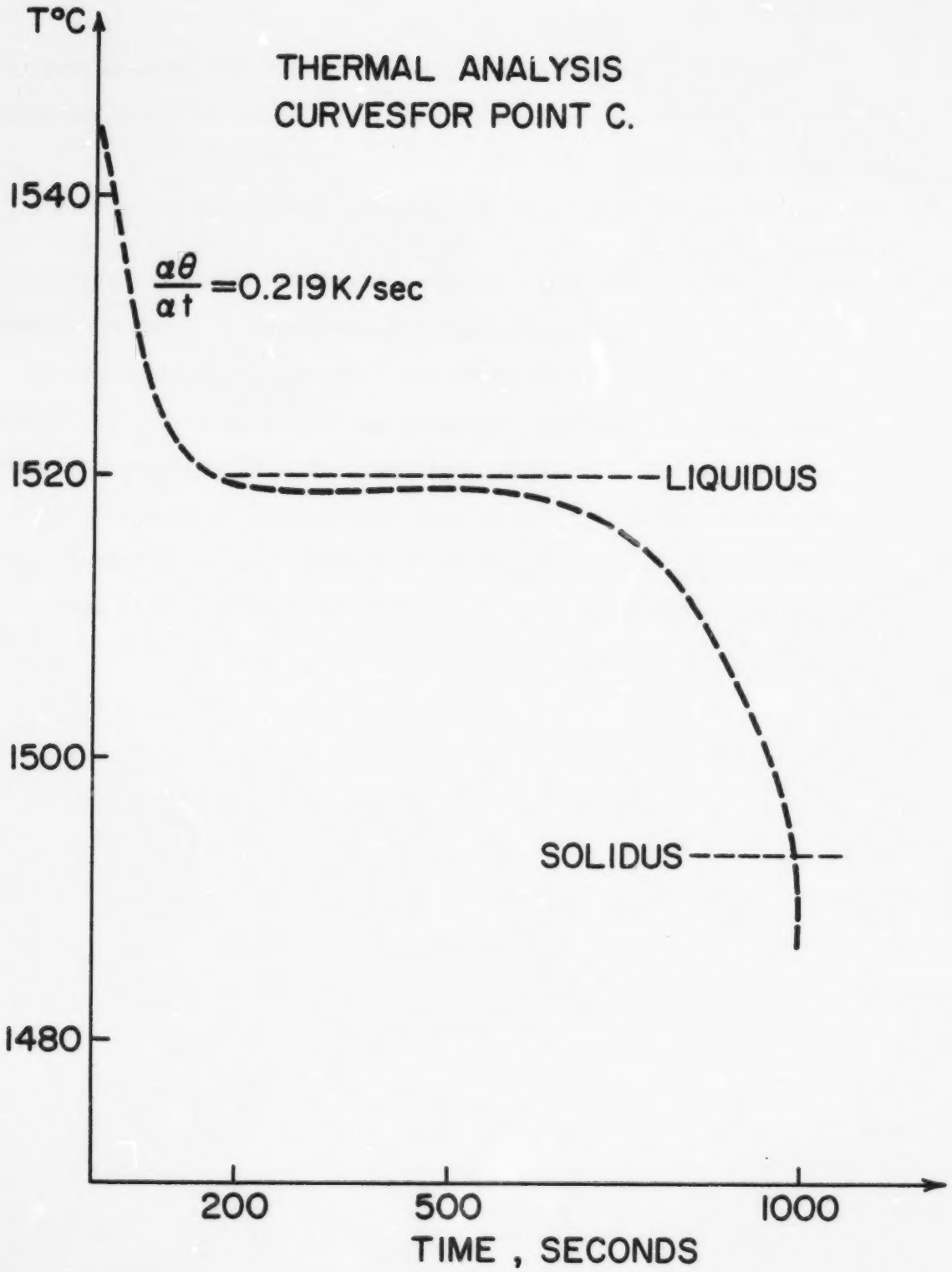
T°C
THERMAL ANALYSIS
CURVESFOR POINT C.
1540
$\frac{\alpha\theta}{\alpha t}$ =0.219K/sec
1520
LIQUIDUS
1500
SOLIDUS
1480
200
500
1000
TIME , SECONDS

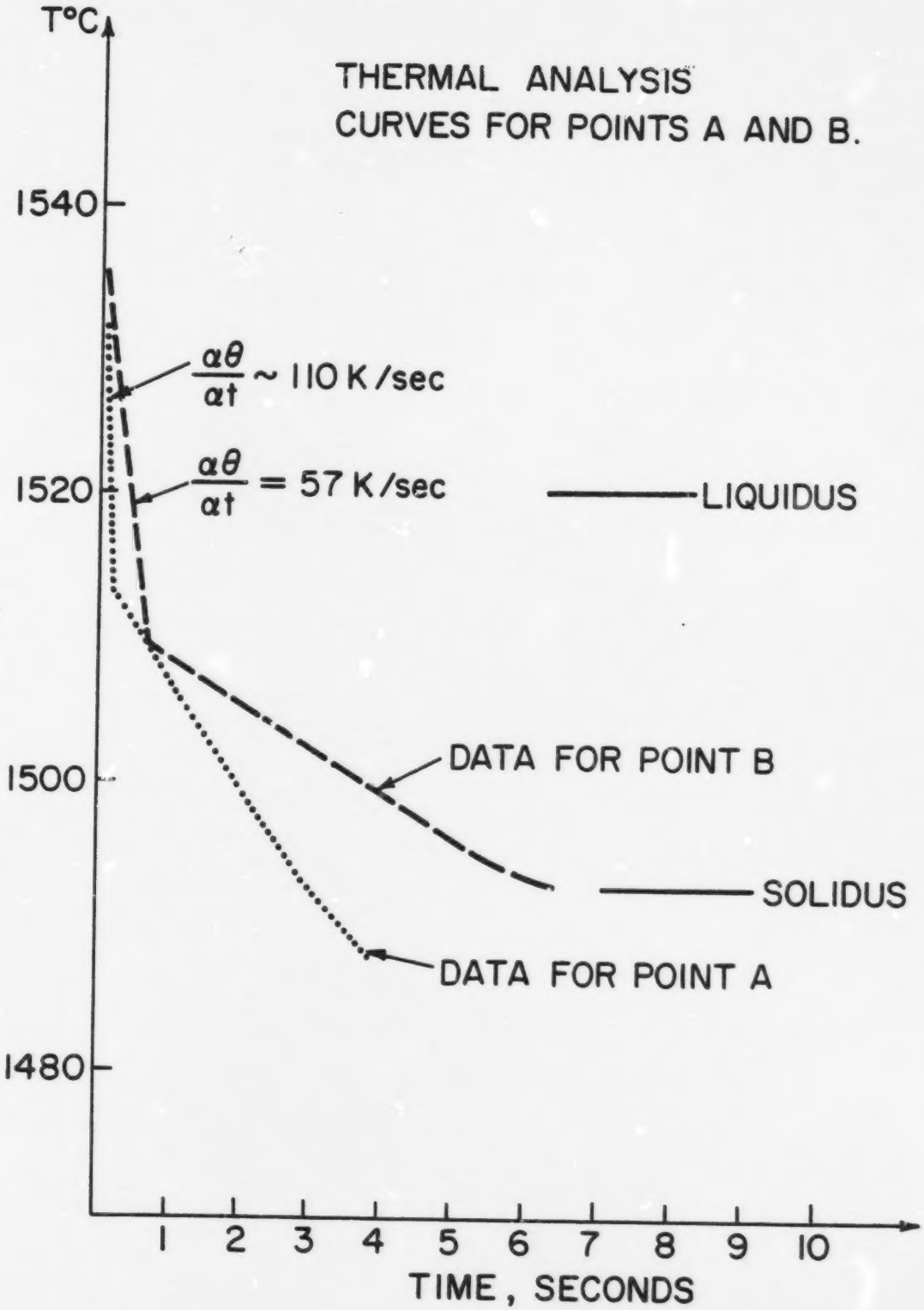
T°C
THERMAL ANALYSIS
CURVES FOR POINTS A AND B.
1540
1520
1500
1480
$\frac{\alpha\theta}{\alpha t}$ ~ 110 K/sec
$\frac{\alpha\theta}{\alpha t}$ = 57 K/sec
LIQUIDUS
DATA FOR POINT B
SOLIDUS
DATA FOR POINT A
1 2 3 4 5 6 7 8 9 10
TIME, SECONDS

Results

A. Influence of Solidification Rate

In order to study the influence of the rate of solidification, experiments were conducted on an alloy whose composition was 0.06% C, 0.0155 Ti, 0.011% N, 0.065% Nb. The cooling schedules used in the study are summarized in Table I.

Table I

Designation	Thermal History
I	cooling rate at freezing point $\sim 140^{\circ}$/min cooling rate at 1200°C $\sim 68^{\circ}$/min
II	cooling rate at freezing point $\sim 52^{\circ}$/min cooling rate at 1200°C $\sim 16^{\circ}$/min
III	cooling rate at freezing point $\sim 10^{\circ}$/min cooling rate at 1200°C $\sim 5^{\circ}$/min

Carbon extraction replicas were produced by standard methods; however, it was found that for materials II and III the replicas showed a marked tendency to fragment yielding on small areas suitable for STEM studies.

Optical micrographs illustrating the basic features of the structures produced by the various cooling rates are shown in Figure 3. It should be noted that (Figure 3a) ferrite grains outlining the prior γ boundaries can be clearly seen. At higher magnification (Figure 4) traces of

precipitates outlining the prior γ boundaries can be seen. Analysis of the replicas indicates that the particles occurring at the prior γ boundaries are often dendritic or irregular in form and of the order of 200 nm in dimension.

The salient feature of the STEM study was that three types of particles were observed. These are illustrated in Figure 5. The dendritic type of particles were only observed in sample I (i.e. the highest cooling rate). The star-shaped particles were often distributed in lines; this may indicate that they nucleate preferentially on dislocations but at present there is no direct evidence to substantiate this possibility. These particles were of the order of 100 nm in size and appear to be cube shaped with pyramids developed on the {100} faces. The small particles were of the order of 20 nm in dimension.

In the STEM X-ray analysis was conducted to determine the % Ti for the various types of particles and its variation with solidification rate. Two important features were found from the STEM analysis. For a given solidification rate the % Ti was essentially the same in all the particles regardless of their dimensions. However, it was found that the titanium content varied systematically with cooling rate from 8.7 in I and 8.4 in II, down to 5.7 in III.

Thus it appears that the Ti content of the precipitates is determined by the Ti and Nb contents remaining in the matrix after solidification. Hence, if the original Ti/Nb ratio is 0.23 and, for example, the ratio observed in precipitates in sample I is of the order

of 0.09, then 60% of the titanium must have been removed as coarse TiN produced in the liquid. Hence, studies of the detailed process of solidification are of importance both in considering the optimization of the titanium level and the tendency to precipitation of dendritic particles at prior γ boundaries. Further consideration should also be given to the ability to control whether the initial solidification structure consists of δ or γ dendrites because this also will clearly influence the initial precipitate distribution and may also determine the Ti/Nb ratio in the particles.

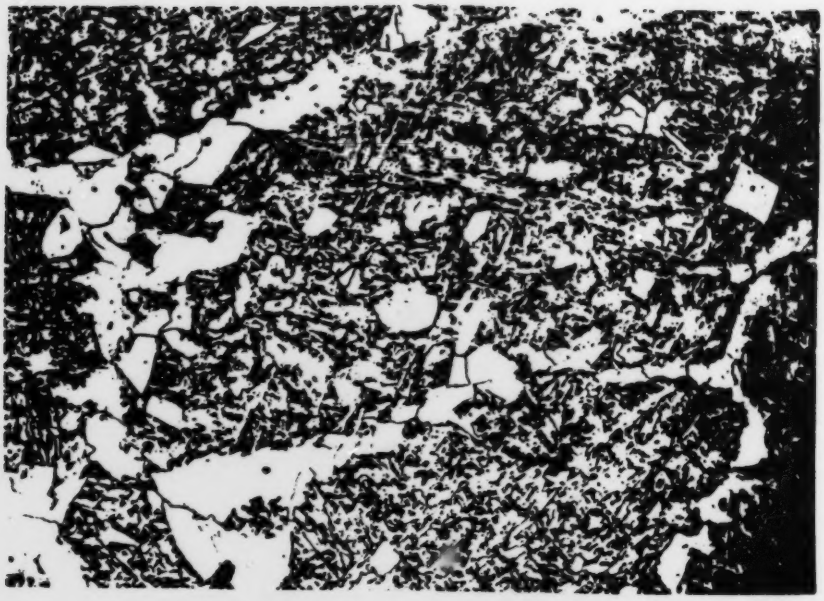

Fig. 3(a) Material I mag. 150X

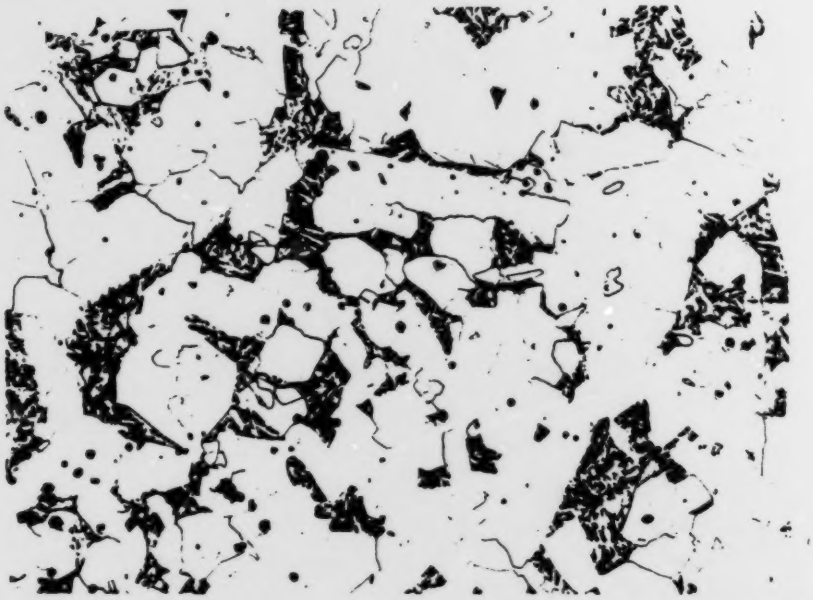

Fig. 3 (b) Material II mag. 100X

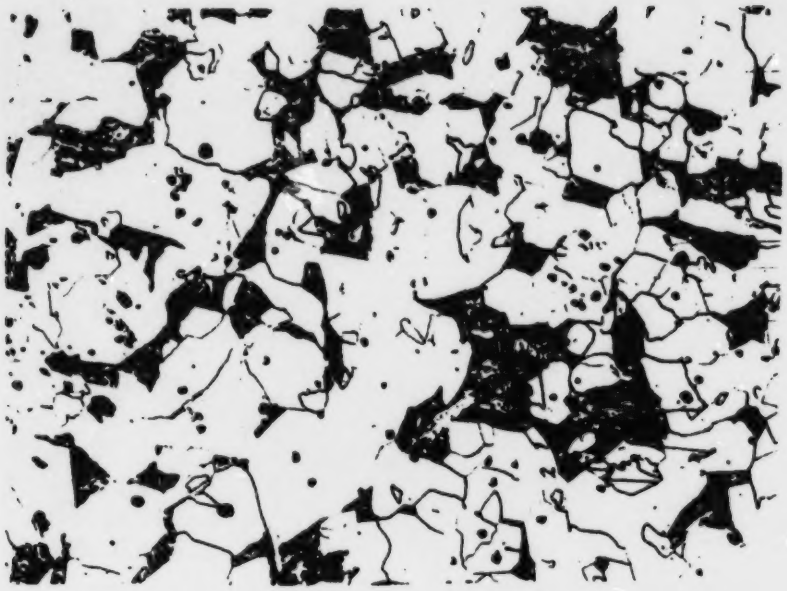

Fig. 3(c) Material III mag. 100X

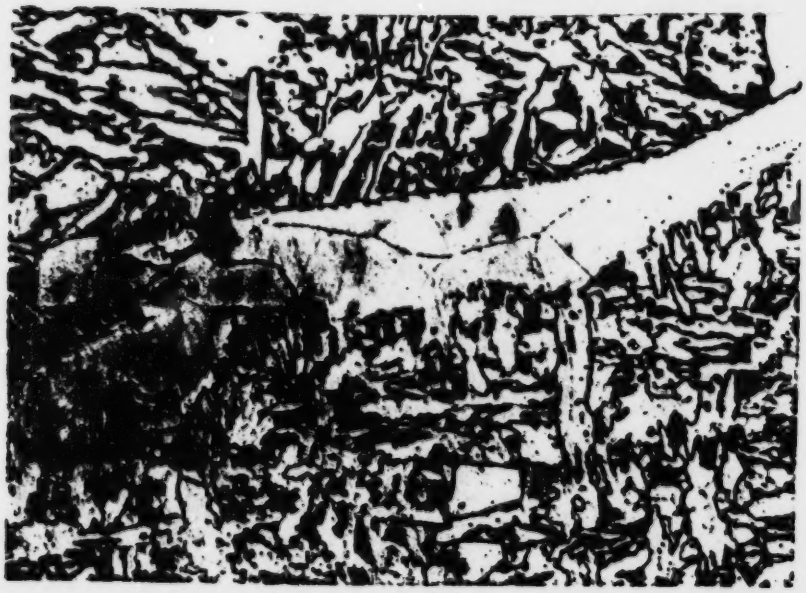

Fig. 4(a) Material I mag. 500X

Fig. 4(b) Material II mag. 500X

Fig. 5 Electron micrographs showing the morphology of precipitates. Magnifications are indicated by n.m. marks.

B. Isothermal Reheat Experiments

A series of reheat experiments were conducted in the range 950 to 1450°C. Carbon replicas were prepared and the Ti/(Ti+Nb) ratio measured using energy dispersive analysis. The most important feature to emerge from this portion of the study was to compare the behaviour of the as-cast material which was reheated and water quenched, with material which was subject to two successive reheat cycles, the first at 1450°C for 4 hours followed by water quenching and the second a reheat to a temperature in the range 950 - 1450°C followed by a final quench. The results of these reheat cycles are summarized in Figure 6. The separation between the two sets of data indicates that on the first reheat cycle some Ti (and nitrogen) is precipitated thus removing it from further involvement in precipitation processes at lower temperatures. Thus on the second reheat the material behaves as though it had much lower effective Ti and N levels. The single reheat experiments indicate that the Nb rich TiNbCN dendrites discussed in previous reports evolve into stable Ti rich particles high in the austenite range (at reheat temperatures greater than 1200°C) and into Nb rich particles at lower temperatures. This is in qualitative agreement with the predictions of the model of the precipitation sequence discussed in the attached report by Houghton, Weatherly and Embury.

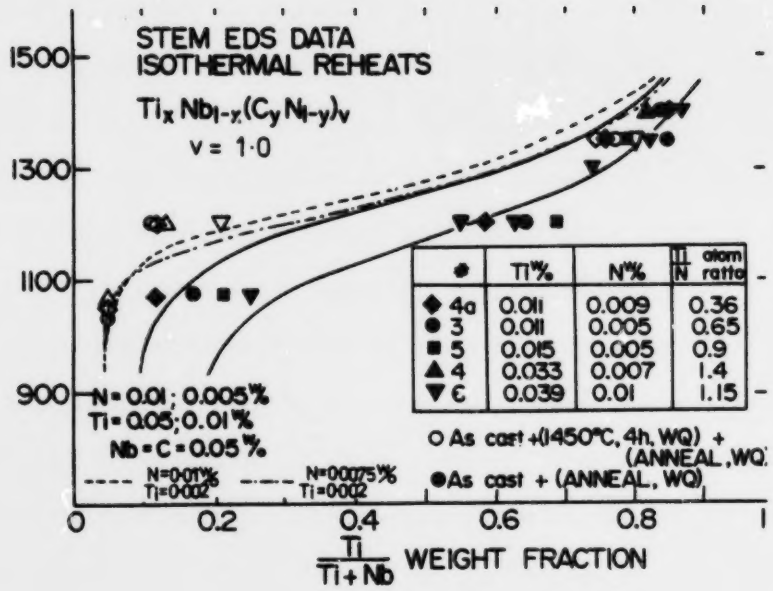

#	Ti%	N%	Ti/N atom ratio
◆ 4a	0.011	0.009	0.36
● 3	0.011	0.005	0.65
■ 5	0.015	0.005	0.9
▲ 4	0.033	0.007	1.4
▼ C	0.039	0.01	1.15

Fig. 6 Diagram showing the variation of Ti/(Ti+Nb) ratio with reheat temperature.

C. Characterization of Carbo-nitrides by Electron Energy Loss Spectroscopy

In the current study one of the most salient features determined to date by the STEM method has been the inherent heterogeneity of the precipitation sequence involving combinations of microalloy elements, although some progress can be made toward further characterization of the nature of precipitate particles using microdiffraction to determine accurate lattice parameters. However, in order to provide a definite measure of C/N ratio it is necessary to develop a reliable analytical method based on electron energy loss spectra (E.E.L.S.) This technique is very demanding in regard to allowable sample thickness and the need to establish well characterized reference materials. It is clear from the data given in Table II that the use of Nb as a standard on which to form carbo-nitrides will present undue difficulties due to the proximity of Nb, M lines and the K lines of C and N. Thus, we are currently developing a technique to produce carbo-nitrides of Cr in order to analyze the relative amounts of C and N. These samples will be prepared by evaporating onto a glass or NaCl substrate, carburizing and nitriding in situ so that suitably uniform thin foils can be obtained and characterized using X-ray methods prior to dissolving the substrate and characterizing the foils using E.E.L.S. It is anticipated that some difficulties will occur due to entrainment of oxygen during the evaporation process.

In addition to the evaporation method described above a technique has been developed to form VC, VN and V(CN) by annealing vanadium foil in

contact with graphite powder at 1050°C for 8 hours. The samples are then placed in a molybdenum wire cradle and annealed in a nitrogen stream at 1070°C for 8 hours. The samples are then ion thinned using a 15° bombardment angle. The ion thinning step needs approximately 24 hours but produces fairly uniform foils which can be characterized by lattice parameter measurements using strips of evaporated gold on the sample to yield reference patterns.

Table II

Data for Electron Energy Loss Spectroscopy

Element	Nature of Line	Energy (eV)
C	K	284
N	K	400
O	K	532
	L_1	24
Nb	M_1	468.4
	M_2	378.4
	M_3	363.0
	M_4	207.0
	M_5	204.6
Cr	L_1	695
	L_2	584
	L_1	74

D. Metallographic Methods

The objective of the metallographic study was to determine the evolution of the microstructure and the location of microalloy precipitate particles in relation to the process of evolution.

Two new etching methods have been developed. The first uses a solution of 140 cc saturated picral, 12 cc of 10% $FeCl_3$, 1 cc of HCl and 2 cc of photoflow. This solution is mixed 1:1 with liquid detergent and used to etch up the prior austenite structure. A second method of revealing decorated prior austenite boundaries was to use a solution of 80% H_2O_2, 5% HF and 15% water. An example of a structure etched with this solution is shown in figure 7.

The structure of the steels listed in the table below have been studied thus far in the program.

Table of Compositions

Alloy Code	C	S	P	Si	Mn	Al	Mo	Ti	Nb	N	Ti/N
449	0.070	0.004	0.003	0.23	1.80	0.025	0.31	0.011	0.005	0.006	1.83
453	0.065	0.004	0.003	0.24	1.74	0.03	0.32	0.010	0.060	0.006	1.67
454	0.075	0.003	0.003	0.23	1.85	0.02	0.31	0.010	0.04	0.006	1.67
460	0.075	0.003	0.003	0.22	1.78	0.028	0.31	0.011	0.01	0.006	1.83

The difference between the edge of the laboratory ingot and the centre are clearly shown by figures 8 and 9. The edge structure shows an elongated primary structure (figure 8) and the centre shows a more equiaxed structure (figure 9). In some cases (figure 10) it can be seen that the form of the

ferrite adjacent to the primary boundaries is very different in morphology from that within the grains. Also phase contrast observations indicate that the picral based etchant is able to reveal substructures within the ferrite as shown in figure 11. This effect appears to arise due to a segregation (or precipitation) effect similar to that discussed by McLean (Grain Boundaries in Metals, p. 141, Oxford Press). The current portion of the work is aimed at quantifying the scale of the primary structures and correlating the optical structure discussed in this section with detailed extraction replica and TEM studies of particle distributions in the cast material.

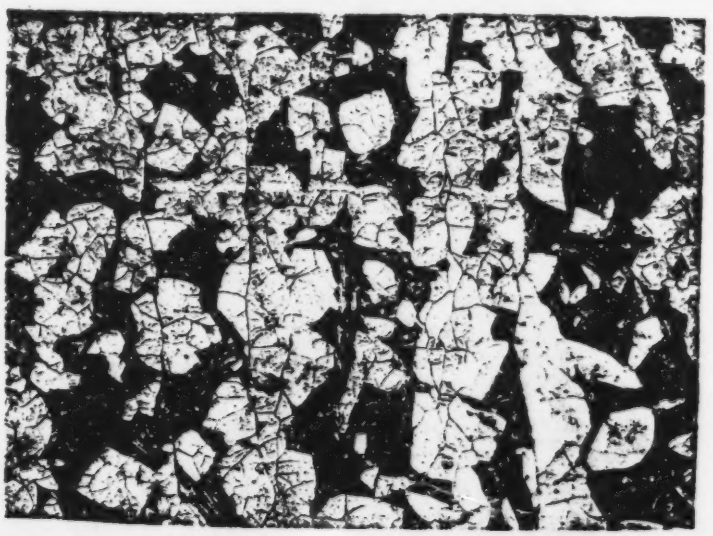

Figure 11: A phase contrast micrograph at magnification X63 showing extensive substructures within the ferrite grains.

Figure 7 A structure from steel 454 showing the etching of decorated prior austenite boundaries achieved with the hydrogen peroxide etching method (magnification X120).

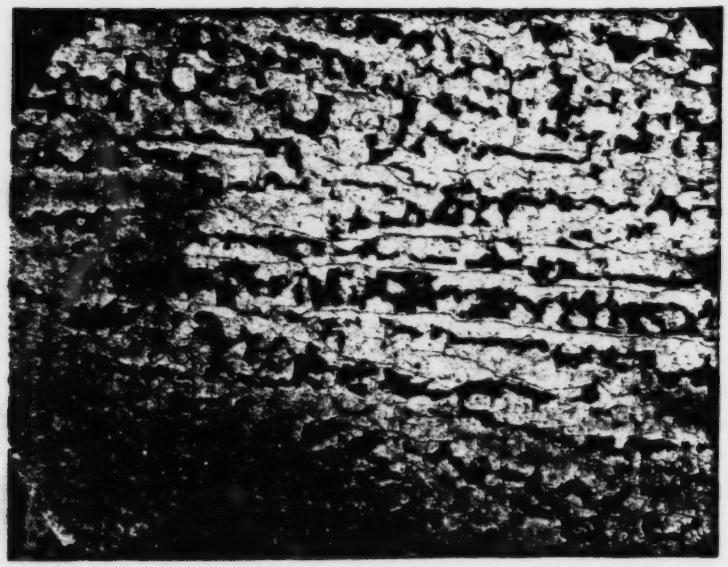

Figure 8 Optical micrograph of the edge portion of alloy 460 showing the relation of the ferritic and non-ferritic constituents to the elongated primary structure (magnification X30).

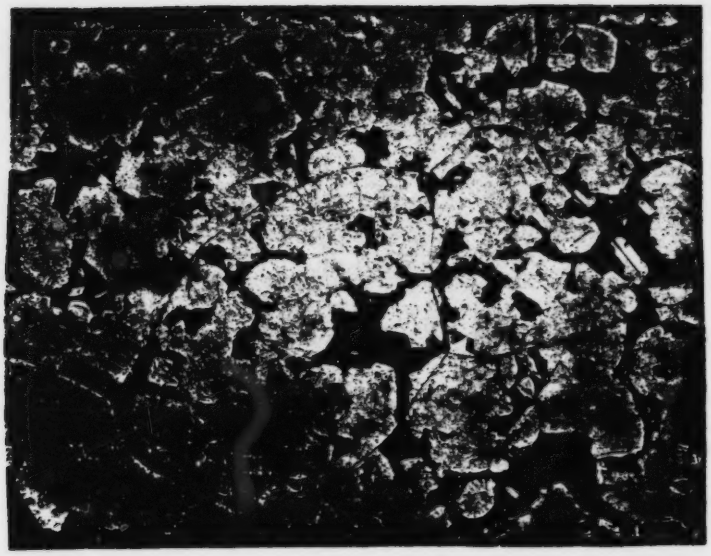

Figure 9 An optical micrograph showing the centre portion of alloy 460 with an equiaxed primary structure (magnification X30).

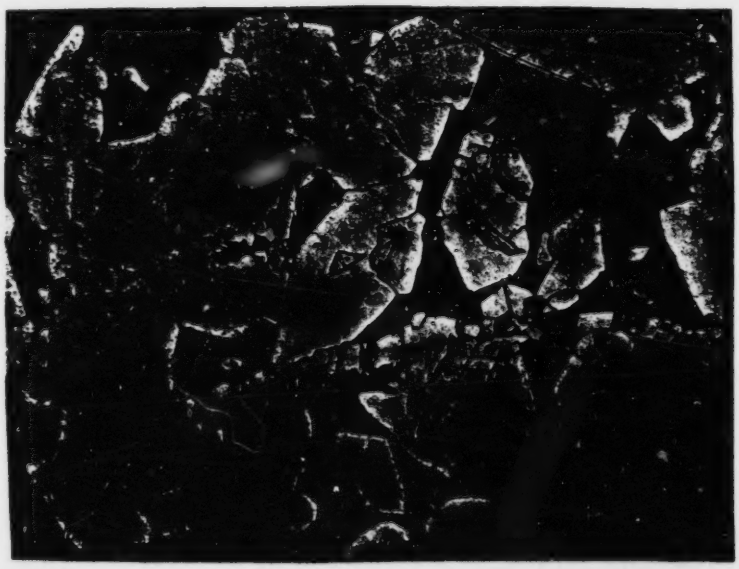

Figure 10 An optical micrograph of the centre portion of alloy 449 showing the difference in the form of the ferrite formed adjacent to the primary boundary (magnification X120).

Industrial Relevance

The form of the initial precipitation of Ti rich particles during solidification has direct relevance to the development of appropriate H.S.L.A. steel technology in Canada. Japanese workers (Suzuki, Nishimura and Yamaguchi, Trans. I.S.I. Japan, 1982, 22, 48) have shown that the precipitation of Nb rich carbo-nitrides at γ grain boundaries coupled with the formation of films of pro-eutectoid ferrite at the γ grain boundaries enhances zone 3 cracking in continuously cast products. This condition can be averted by judicious choice of alloying levels, modification of ferrite formation by Mo and limiting the initial hot rolling deformation.

A further important feature is that the level of microalloy element plus the cooling rate determines whether the initial dendrites are δ or γ. High levels of Nb tend to increase the tendency to the formation of γ dendrites which yield a product which is not amenable to direct rolling treatments (Dr. Subramanian, private communication). Callmer and Grinder (Scand. J. Metallurgy, 1974, 3, 69) have developed a thermal analytical method for ferritic stainless steels containing 0.27 to 0.60 Ti and 0.006 to 0.012 N which is capable of detecting the formation of primary TiN. Clearly in view of the results reported in section A of this report it would be of value to determine whether this method is capable of yielding data on the formation of primary TiN in HSLA steels.

Further, in order to clarify the temperature ranges of formation of the non-ferritic transformation products occurring in the Ti/Nb HSLA steels,

it would be of value to characterize the weld cycles by dilatometric methods in order to supplement the microstructural data yielded by the current S.T.E.M. and T.E.M. study.

The data reported in section B concerning the role of the initial reheat at 1450^{o}C on the reduction of the effective level of Ti and N available in subsequent precipitation reactions may be of relevance to the observations reported by previous workers that multiple thermal cycles in the H.A.Z. region reduce the grain refining efficiency of Ti. This is worthy of further study using multiple Gleeble cycles in conjunction both with S.T.E.M. studies of precipitate distribution, determination of prior γ grain size and H.A.Z. toughness studies. However, it must be recognized that S.T.E.M. data alone is insufficient because one major weakness of the current S.T.E.M. studies is their inability to yield reliable data concerning volume fractions of precipitate particles.

The Microchemistry of Carbonitrides in the Heat Affected Zone of H.S.L.A. Steels

D.C. Houghton, G.C. Weatherly & J.D. Embury
Univ. of Toronto-McMaster Joint STEM Facility
Dept. of Metallurgy & Materials Science
McMaster University
Hamilton, Ontario, Canada

Abstract

The characterization of precipitates in a series of Ti bearing HSLA steels has been carried out using a dedicated STEM instrument. Microanalysis utilizing a simultaneous combination of EDX, EELS and micro-diffraction techniques has allowed unequivocal precipitate identification. Excellent spatial resolution and high precision microchemical analysis have been achieved using extraction replicas. The range of particle sizes analyzed was from ∿3 nm up to several micrometers. The influence of titanium concentrations from zero up to 0.39 w/o was investigated in laboratory cast steels made from electrolytic iron of nominal composition 0.06 w/o C, 0.01 w/o N, 0.05 w/o Nb, 0.3 w/o Si, 0.3 w/o Mo and 1.85 w/o Mn.

The thermomechanical process conditions for each heat were maintained constant. In a previous study all steels were examined in the as cast, isothermally reheated and control rolled conditions. These provided a basis for the study of structures developed in the heat affected zones of submerged arc welded plates. These regions were studied by mapping the

distribution of precipitates as a function of distance from the fusion line. The ferritic microstructures obtained in the HAZ were correlated with the morphology, spatial distribution and microchemistry of carbo-nitride precipitates. The major portion of the present study was devoted to the characterization of the carbonitrides present in the heat affected zones and their stability with respect to various thermal cycles. The precipitate stability, redistribution of micro-constituents during thermal cycles and the role of carbonitrides in grain size control are discussed. However, it should be emphasized that the processes occurring during weld cycles can only be understood by studying the evolution of the precipitate morphology and distribution during the whole sequence which follows casting. The current study indicates that the niobium rich dendritic morphology of particles typically found in as cast microstructures decays during iso-thermal reheating in favour of titanium rich precipitates, some of which appear to be composite particles which suggests a precipitation sequence where two or more temperature regimes predominate.

Introduction

The development of weldable high strength, microalloyed steels with an attractive toughness-strength ratio has resulted from an improved understanding of the interrelationship between microstructure and mechanical properties.[1,2] The role of transition elements, even in concentrations << 1 w/o, e.g. Ti, Nb and V, during thermomechanical processing[3,4,5] and fabrication,[6] is complex. However, the precipitation of stable carbonitride compounds during successive stages of processing is well established and has been the subject of several experimental investigations.[7,8,9] The contribution of individual pairs of precipitating elements, e.g. Nb and C, forming binary compounds to the development of final mechanical properties has been reasonably well documented.[3,10] The subtle differences in solution behaviour and the relative stabilities of the carbonitrides of the three major microalloying elements, Ti, Nb, V, have been discussed by Meyer et al.,[3] and more recently by Honeycombe.[11]

The solubility of single binary compounds in ternary iron alloys has been studied by many investigators for most of the compounds likely to precipitate during processing of microalloyed steels.[10,12,13] In contrast, very few experimental studies[10,14,15] or theoretical attempts[16,17] have been made to quantify the interaction of more than two solutes.

Several authors[18,19,20] have reviewed the physical and chemical characteristics of transition metal-interstitial alloys. Complete solid solubility has been found for the groups IVa and Va microalloy carbonitrides, having the rock-salt structure, and a continuous range of physical

properties from one pure compound to the other is possible.[18] The thermochemical data for this intermixing of compounds, however, has not yet been documented.

In order to delineate the precipitation sequences operative when several microalloying elements are simultaneously present, two approaches are adopted in the current work. The precipitation reaction was followed experimentally by characterizing the composition of the particles extracted at various stages during processing and heat-treating of the alloys. This characterization can only be adequately performed by using the high resolution microanalysis capability of a dedicated STEM. Secondly, the combined effect of the microalloying elements have been treated in models which utilize simplifying thermodynamic assumptions, i.e. negligible interaction between precipitating compounds or the assumption of an ideal solution of precipitates in the formation of a complex carbonitride, $Mi(X_j)_v$.

The basis of the model and its predictions relating to the volume fraction of precipitates formed as a function of temperature have been treated in detail in a recent conference paper.[15] It should be noted that although the models are of value in predicting the simultaneous role of microalloying elements such as Ti and Nb they do not, in their present form, take cognizance of the local initial variations in composition which may form the average bulk composition due to macrosegregation. This shortcoming is important particularly in relation to the compositional inhomogeneities inherent in continuously cast products which may lead subsequently to important variations in the nature and distribution of

the carbonitrides responsible for grain size control.

Despite these limitations of the model it is of value to consider in a quantitative sense its prediction regarding the stability of various microalloy phases with respect to soaking cycles, hot working and the thermal cycles associated with welding. In the present study the precipitate characterization based on STEM analysis was found to be in basic accord with the thermodynamic model. The results also indicate no substantial differences in composition with a given region for precipitates of the same morphology.

In the present study the emphasis has been placed on studies of the H.A.Z. regions of welds and Gleeble simulation of weld cycles. However, in order to place results of the welded structures and Gleeble simulated structures in context, it is necessary to review briefly the salient features of the microstructure produced by the various operations prior to welding and this review is included in a later section.

One of the important potential benefits of Ti additions of HSLA structural steels is to provide a mechanism for austenite grain size control during welding.[21-24] The present work examines the role of titanium in grain size control and the stability of the various carbonitrides present in the as rolled plate with respect to the thermal history of weld cycles. In addition, consideration was given to the need to optimize reheat cycles prior to hot rolling for alloy steels containing combinations of Ti and Nb and hence consideration was also given to the influence of abnormally high reheat cycles and precipitate stability.

Experimental Procedure

a) Materials Preparation and Processing

A total of seven experimental steels were air-induction melted using electrolytic iron and cast as ∿68 kg rectangular ingots with dimensions 127 x 203 x 254 mm. The base chemical analysis of these steels was typical of a Mo and Nb-bearing, partially acicular, ferrite steel suitable for line pipe applications required a 500 MPa yield strength. Nitrogen and titanium additions were made to the base chemistry as indicated in Table I. Two nitrogen levels (0.012 and 0.006 w/o N) were used in order to relate the studies to the practical process of CAB desulphurization since this later process is found to increase the BOF nitrogen content by a factor of two. The titanium level was varied from zero up to 0.039 w/o to obtain a range of stoichiometry from excess nitrogen to excess titanium (expressed in terms of the atomic ratio). Control of titanium and nitrogen concentrations was difficult, presumably due to reoxidation during ingot pouring and concomitant solute interactions in the melt.

The casting practice was designed to simulate commercial continuous casting practice. Casting into sand moulds with iron chills on two opposing faces was designed to give a range of cooling rates closely resembling that obtained in strand cast slabs. Cooling rates of $\sim 16^{\circ}C\ min^{-1}$ at the surface and $\sim 9^{\circ}C\ min^{-1}$ at the ingot centre at the solidus temperature were achieved. Each ingot was sectioned and analyzed for chemical homogeneity, although no macroscopic variations were detected. The reheating practice involved heating to a maximum temperature of $1220^{\circ}C$ within 2 hours and holding at

that temperature for 2 hours prior to control-rolling.

Half of each sectioned ingot was control-rolled from a slab of dimensions 130(thickness) x 150(width) x 1250 mm to ∿15 mm thick plate. The drafting schedule consisted of 10 roughing passes to ∿63 mm at temperatures between 1095°C and 925°C, followed by finish rolling which involved a 75% total reduction obtained by 9 passes between 885°C and 775°C. Plates were then air cooled to ambient temperature.

To investigate the influence of abnormally high reheat temperature, laboratory isothermal anneals were all carried out on ∿13 x 13 x 13 mm test pieces machined from as-cast sections. The test pieces were sealed off in an inert gas atmosphere in quartz capsules prior to heat treatment for times between 1 hour and 16 hours at temperatures in the range 1100 - 1450°C. After isothermal exposure, each capsule was broken under iced brine.

b) Welding and Gleeble HAZ Simulations

Coupons of as-rolled plates from different heats were double-pass submerged arc welded using standard edge preparation, consumable electrodes and welding parameters chosen to closely parallel the commercial welding operation during pipe fabrication. The heat input was typically 2 kJ mm^{-1}.

In addition, test pieces 10 x 10 x 55 mm were machined from rolled plates suitable for thermal cycling in a Gleeble 510 weld simulator. The thermal pulse was designed to reproduce that of a single pass SAW thermal input 2 kJ mm^{-1}, attaining a peak temperature of 1350°C ± 10°C within 6s,

a dwell time at 1000°C of 8 ± 1 sec and a characteristic cooling time between 800 and 500°C of 26 ± 2 sec. These temperature-time characteristics are presented schematically in Figure 1.

c) Optical Metallography

Standard mechanical abrasion and diamond polishing techniques were used to prepare specimens prior to etching for optical microscopy, austenite grain size measurement or carbon extraction replication. Etching for optical microscopy was done using 10 v/o nitric acid in ethanol for 10 sec at ambient temperature. To reveal prior austenite grain boundaries in both thermally cycled plates and annealed specimens aqueous picric acid saturated with a wetting agent was used. Prior austenite grain sizes were measured using the linear intercept technique.

d) Extraction Replicas and Conventional Transmission Electron Microscopy (CTEM)

Conventional techniques of etching in 2 v/o nital, carbon evaporation and stripping with 5 v/o nital were adopted followed by repeated washings in de-ionized water before being picked up on 200 mesh aluminum or carbon coated nylon grids.

The vigorous reactions involved in stripping the extraction replica often resulted in contamination of the replicas by layers of iron rich oxides. Thus, in order to avoid spurious signals in the process of microchemical analysis any replicas containing obvious clusters of oxide were rejected. A precise replica technique needed to be developed for the

analysis of precipitates and other microstructural features as a function of radial distance away from the fusion line through the CG HAZ. Rectangular strips spanning the whole heat affected zone were taken from selected specimens, as shown schematically in Figure 2. Masking off the unwanted regions allowed the desired areas to be replicated. The position of the fusion boundary in each replica was readily identified by the presence of large silicate inclusions clearly visible within the fusion zone. This technique allowed systematic analysis of regions where the peak temperature attained during the weld thermal cycle is progressively reduced. The spatial distribution of particles and their influence on local ferrite morphology could then be correlated directly. In parallel with this study, the prior austenite grain size was measured optically as a function of distance from the fusion boundary.

A layer of evaporated gold approximately 20 nm in thickness was laid down on selected replicas, in order to provide a standard for the determination of precise lattice parameters. Lattice parameter determination with an absolute accuracy better than ±0.5% was possible using SAD techniques in a Philips EM 300, CTEM.

e) STEM Microanalysis

The unique capabilities of 'dedicated' STEM microscopy allow the quantitative microanalysis of isolated precipitates in the size range 2 nm up to ∿5 μm. The absolute accuracy of EDS X-ray techniques using a Vacuum Generator HB5 instrument equipped with a Kevex 7000 system was found by the use of thin film standards to be better than ±5%. The minimum detectable

mass in this microanalytical configuration was $\sim 10^{-20}$ g which corresponds to approximately 100 atoms of microalloying element. The point to point spatial resolution of the X-ray system has been shown to be $\lesssim 5$ nm.

The vacuum at the specimen during microanalysis is $\lesssim 10^{-8}$ torr and contamination during analysis was minimized by use of an infrared thermal cycle performed in situ prior to examination.[28] The specimen holder was made of beryllium, and all microscope components in the vicinity of the sample were of low atomic number material to minimize the Bremsstrahlung signal. A hole count of $\sim 1/4$ C S^{-1} is readily achieved at an X-ray take-off angle $\sim 40^{o}$, while the total count rate from a region of replica containing no vibible precipitates was <1 C S^{-1}.

Continuum background subtraction was performed by building a cumulative model of all acquired spectra in each data set. Then by fitting a polynominal curve to this grand mean and normalizing to individual spectra good background correlation was attained prior to stripping and analysis. Quantitative analysis of the X-ray data was performed by the assumption of the thin film criterion and application of the well-known Cliff-Lorimer ratio technique.[25] This produced reproducible data and uncertainties of $\sim 5\%$ or less were obtained. Scatter in measured chemical composition greater than this value was attributed to actual composition variations in the precipitates.

Simultaneous microdiffraction and electron energy loss spectroscopy were also carried out during EDS X-ray microanalysis to determine the crystal symmetry and orientation, and to estimate the light element content.

The use of a microdiffraction technique to track extremely small precipitates ($\sim$ 2 nm) during X-ray data acquisition[26] is essential since combined thermal and electronic drift cannot be completely compensated at magnifications of 2.5×10^6.

The role of Al, Si, Mo, Fe and Mn in carbonitride formation was extensively studied during STEM EDS analysis. No significant Al concentrations were detected in any of the precipitates analyzed. In control-rolled microstructures, small concentrations of Mo and Fe were found in the finest precipitates ($\lesssim$ 20 nm). These may have been due to a surface layer effect induced during austenite decomposition, as a result of preferential nucleation of Mo_2C and Fe_3C at the pre-existing matrix/carbonitride interfaces. No evidence for silicon or manganese in precipitated compounds of the form MX_y was found. Their only influence on precipitation is thus likely to be through modification of the solute activities.

Review of Precipitate Development

In order to describe the precipitation sequences occurring in the presence of two or more microalloying additions such as Ti and Nb, models have been developed, as discussed in a previous publication,[15] based on a) co-precipitation i.e. no mixing of the precipitating species or b) complete intersolubility of the precipitating compounds. The results of these two types of models are illustrated in Figure 3 for a steel containing Ti below the level for stoichiometric nitrogen balance.

Essentially, three approaches to the analysis have been superimposed in this figure to illustrate the separate and combined effects of mixing the transition elements and interstitial components on a single lattice. At any one temperature the mole fraction of precipitate is found to be significantly higher as intersolubility is allowed to take place.

The variation of transition element to light element ratios in the complex compound Ti_xNb_{1-x} $(C_yN_{1-y})_v$ is presented in Figure 4. The tendency to form titanium nitride at high temperatures and niobium carbide as precipitation goes to completion at lower temperatures is clearly demonstrated. This is an important feature because it indicates that the roles of the microalloying elements may be separable in that Ti may be effective as a precipitate during reheat cycles and high temperature thermal cycles in welding but the behaviour at lower temperatures for example in recrystallization during hot rolling may be dominated by the compounds of niobium. Mixing of the compounds creates compounds of the form $Ti_xNb_{(1-x)}$ (CN) which go into solution at a different temperature than NbC as illustrated in Figure 3.

Let us now consider the sequence of changes occurring during reheating and controlled rolling.

a) Isothermal Reheat Experiments

In order to rationalize the morphological changes occurring on reheating the as-cast structures, a series of isothermal anneals were carried out at a single Ti concentration of 0.039 w/o, heat #5. The holding times at various temperatures up to 1450^{o}C were selected so that

equilibrium could be attained both inside the precipitates and throughout the austenite matrix.

The precipitate geometry can be seen to follow a regular sequence from an as-cast feathery 'dendrite' character (Figure 5a) through an intermediate morphology on heating at ∿1200°C (Figure 5b) to the facetted cuboidal geometries of particles found at 1300°C (Figure 5c) D and at higher temperatures 1400°C (Figure 5d) D. No detectable precipitates were found in the sample which was reheated at 1450°C for 4 hours.

The austenite grain coarsening behaviour and the corresponding STEM microanalysis of equilibrium precipitates are listed in Table II as a function of annealing temperature.

The EDS X-ray data clearly show the increase in Ti concentration in the precipitates with increase in reheat temperature. The utilization of Selected Area Diffraction measurements of lattice parameters in combination with the precise Ti/Nb ratio obtainable by STEM EDS measurements allows the $(\frac{N}{C + N})$ ratio to be determined as shown in Figure 6.

The existence of a stable Ti-rich nitride precipitate at higher temperatures is in accord with the predictions of a model based on intersolubility of the precipitating species as shown in Figure 7.

Control Rolled Microstructures

The ferrite morphology and precipitate distribution in all the Ti heats were very similar. The ferrite grain size was ∿5.0 μm in Ti-bearing heats and ∿6.0 μm in the steel containing no Ti. However, a more homogeneous and slightly finer ferrite grain structure was noted in steels

containing low Ti concentrations (0.005, 0.01 w/o) and this accompanied by a higher volume fraction of polygonal ferrite was attributed to the finer, more uniform austenite grain structure prior to transformation. The steels containing low Ti concentrations also exhibited higher toughness, as indicated by a lowered FATT measured by the Charpy impact test.[6]

The STEM microanalytical data is summarized in Table III and typical precipitate morphologies are shown in Figure 8. The precipitate size distribution was clearly bimodal containing large cuboidal precipitates $\sim$(50-200)nm and a homogeneously distributed fine precipitate $\lesssim$20 nm. No evidence for precipitation taking place preferentially at grain boundaries could be found, nor were precipitate free zones detected around the larger particles.

In the high Ti steels (#3 and #5), extremely large well-defined cubes $\lesssim$1 μm in edge length gave rise to only Ti characteristic X-ray signals during STEM EDS analysis. These were considered to be TiN particles produced either in the melt or on solidification, and are presumed to play no further role in the precipitation reaction.

The development of the bimodal distribution of precipitates has probably taken place in two stages. During isothermal reheating the as-cast Nb-rich precipitates decay in favour of the thermodynamically stable Ti-rich nitride compounds of the form $Ti_xNb_{1-x}N_y$. The Ti concentration in these cuboidal precipitates will be a function of the 'available' Ti level in the region of the precipitate, the reheat temperature and the

time available for equilibration. The next stage of this precipitation sequence takes place during the forced cooling cycle imposed by controlled rolling. Insufficient time is available for precipitate homogenization during hot working, and consequently layered or cored precipitate morphologies occur with encapsulation or epitaxial 'cap' growth taking precedence over homogeneous nucleation in the austenite matrix. The epitaxial growth of a Nb-carbonitride cap, as seen in Figure 9, was found frequently in these steels. The strong contrast variation visible in this figure confirms the abrupt change in electron density at the cap-cuboid interface due to the large difference in atomic number between Nb and Ti.

The fine precipitates detected in all heats were predominantly Nb(C,N). These form during the later stages of thermomechanical processing in the temperature range $\sim(1100 \rightarrow 800)^{o}C$ and contain significant Ti concentration in steels with nominal Ti levels greater than the stoichiometric nitrogen concentration.

Heat-Affected Zone Gleeble Microstructures

Heat-Affected Zones

The dispersion of fine carbonitride precipitates seen in the as-rolled structure was not detected in any of the Coarse Grained Heat-Affected Zone structures, i.e. within $\sim$0.5 mm of the fusion line. A few, randomly dispersed, very large cuboid precipitates $\gtrsim$1μm in edge length were found throughout the heat-affected zones of the high Ti heats #3 and #5. These appear to be TiN particles which persist unmodified from the as-cast condition.

In an attempt to correlate the influence of time at maximum temperature with the precipitate distribution and austenite grain growth data STEM microanalysis was carried out on precipitates found within the heat-affected zone by tracking back from the fusion line in the direction of heat flow along extracted strip replicas.

A random distribution of cuboidal precipitates was observed in all Ti heats. Typically, the precipitates varied in size from 20 - 200 nm in edge length throughout the 0.5 mm CGHAZ region studied. The actual precipitate size distribution in the coarse grained HAZ of selected steels are presented in Figure 11. No correlation between mean precipitate size and Ti/N ratio is evident from this data. A significant variation in the Ti content of precipitates was found, even within one region of a replica. Steep concentration gradients were also detected close to the surface of the large cuboids ($\gtrsim$ 100 nm). The STEM EDX X-ray data from a "composite" precipitate found close to the fusion line in steel #5 is shown in Figure 10. A Ti rich skin was frequently detected.

The variations in precipitate composition, together with significant differences in composition between particles, indicate that the thermally cycled precipitates are far from equilibrium and that particle size plays an important role in determining the overall composition. The rate of diffusion within the precipitate is $\sim$4 orders of magnitude slower than the matrix at welding temperatures[27] and hence this should be the rate limiting transport mechanism. Thus for smaller particles the approach to equilibrium is much faster than that for particles $\gtrsim$ 100 nm in size. Fine precipitates can adjust their overall composition and at higher

temperatures may dissolve, reducing the precipitate volume fraction. Larger particles, however, have been found to develop a Ti-rich skin, which may subsequently act as a barrier to further composition adjustment and are thus stabilized during the weld thermal cycle. The absence of Nb-rich spheroidal precipitates and the Nb-rich envelopes found in the as-rolled microstructure suggests that the dissolution of these Nb-rich compounds is more rapid. This is supported by the observation that no precipitates were detected in the HAZ of control heat #1, indicating complete solution of Nb during the thermal cycle.

Within each HAZ investigated, no significant change in precipitate geometry, size distribution or chemical composition could be detected as a function of distance from the fusion line. The relatively uniform distribution of precipitate sizes and compositions within the CGHAZ may be again a reflection of the inability of large ($\gtrsim$ 100 nm) particles to reach equilibrium in the short time available during a weld thermal cycle. Small precipitates may disappear through internal chemical homogenization and dissolution. Large precipitates cannot respond, generate TiN-rich skins and become stabilized. A decrease in the volume fraction of grain refining precipitates is expected close to the fusion line, but even relative estimates of precipitate volume fractions proved to be inconclusive. It was difficult to control the stripping action of the replicas across the heat affected zones and the extraction of precipitates may not bear a linear relationship with the actual precipitate population.

The prior austenite grain size within the CGHAZ of welded plates from all heats has been plotted as a function of distance from the fusion line

in Figure 12. A significant improvement in grain size control is obtained by the addition of Ti, but no obvious choice for the optimum Ti to N balance in the base steel is suggested by the data.

Gleeble Simulation

The time-temperature characteristics of the Gleeble weld simulation thermal cycles are represented in Figure 1. The austenite decomposition products were closely similar to those found in actual heat-affected zones of submerged arc welds.

The prior austenite grain size in the region of maximum peak temperature was measured for all the heats (see Table IV). The results followed the trends already noted in the as-welded samples: a marked improvement in grain coarsening resistance is observed on the addition of Ti, but no optimum Ti level is evident from grain size measurements alone.

The STEM microanalysis of precipitates extracted from Gleebled specimens showed that there was no systematic difference in size, shape or chemical composition between precipitates found in the high ∿0.04 w/o Ti or the low ∿0.01 w/o Ti steels.

The data presented in Table IV was obtained from approximately 50 separate analyses in each case. The scatter both in the chemical composition data and in the size of precipitates reflects the true variation in these parameters. Again it was found that replicas taken from the maximum temperature zone of Gleeble cycled Ti-free heat were free of precipitates.

Summary

The results of the present study have shown that a complex series of precipitation reactions occur during the processing of HSLA steels containing Ti and Nb. At each stage, the distribution and composition of the precipitates is determined by the prior thermal history of the alloy up to that point, as summarized below.

a) As-cast

The as-cast structures of the Ti-bearing heats contained precipitates rich in Nb and N, having a dendritic morphology and ranging in size from ~10 nm to greater than 1 μm in their largest dimension. These precipitates are heterogeneously distributed, many of them apparently lying at grain boundaries.

b) Solution-Reheated

On heating the as-cast alloys, at temperatures $\gtrsim 1100^{\circ}C$, the Nb-rich dendrites are progressively replaced by an array of Ti-rich cuboidal precipitates. As the reheat temperature is increased, the cuboids become increasingly rich in Ti as their composition approaches TiN. This experimental observation supports the conclusions drawn from the models discussed in an earlier section.

The spatial distribution of these cuboids is again heterogeneous, and to some extent this appears to be inherited from the distribution of dendritic particles in the as-cast alloy.

c) After Thermo-Mechanical Processing

During the controlled rolling sequence, further precipitation of Nb-rich carbonitrides occurs, both heterogeneously as 'caps' on the cuboidal precipitates and homogeneously (or heterogeneously on dislocation arrays) in the austenite matrix. The composition of these Nb-rich precipitates is in accord with that predicted by the ideal solution model for Nb(C,N). Insufficient time is available for equilibrium to be attained in the 'capped' cuboids, so that their 'cored' composition is retained to room temperature. The fine distribution of spheroidal Nb-rich carbonitrides ($\sim$ 20 nm in size) will play an important role in the retardation of recrystallization during processing. The coarser distribution of Ti-rich nitrides control austenite grain growth during the weld thermal cycle.

d) Thermal Cyling

Rapid reheating cycles both in the heat-affected zones of submerged arc weld and the Gleeble thermal cycle experiments produced essentially identical results. The first effect of this thermal pulse is to dissolve the fine Nb-rich precipitates produced during control rolling and, after dissolution of the caps, to expose the grain refining nitride precipitates to temperatures which can be in excess of their solution temperature. However, insufficient time is available during a weld cycle to permit complete chemical homogeneity to be established, except for within the smallest nitride precipitates. Consequently, in these "far-from-equilibrium" conditions, many of the small cuboids dissolve while concentration gradients are set up within the larger ones as Nb is taken

into solution from the surface layers.

The efficacy of a precipitate dispersion as a grain refining agent may therefore be as dependent on the mean particle size and size distribution as on the inherent stability of the compounds involved.

Acknowledgements

The authors are grateful to Mr. D. McCutcheon of Stelco for valuable discussions and the staff of CANMET for provision of the Gleeble studies. In addition, the authors are grateful to NSERC, Canada and CANMET for research support, and to the University of Toronto for the provision of a research fellowship to D.C. Houghton.

References

1. F.B. Pickering: Microalloying '75 Proceedings, pp. 9, 32; 1977, Union Carbide Corporation, New York.
2. T. Gladman, D. Dulieu and I.D. McIvor: ibid; pp. 32, 55.
3. L. Meyer, F. Heisterkanp and W. Mueschenb: ibid; Microalloying '75, pp. 153,168.
4. A. LeBon, J. Rotes-Vernis and C. Rossard: Mem. Sci. Rev. Met., 1973, 70, 577.
5. T.M. Hoogendoorn and M.J. Spanraft: Microalloying '75 Proceedings, p. 75; 1977, Union Carbide Corporation, New York.
6. D.B. McCutcheon, J.T. McGrath, M.J. Godden, G.E. Ruddle, G.C. Weatherly and D.C. Houghton: Micon '82 Conference Proceedings, Houston, Texas.
7. H. Watanabe, Y.E. Smith and R.D. Pehlke: 'The Hot Deformation of Austenite', p. 140; 1977, The Metallurgical Society of AIME, New York.
8. A.T. Davenport, R.E. Miner and R.A. Kot: ibid, p. 186.
9. S.S. Hansen, J.B. Vandersande, and M. Cohen: Met. Trans. A, 1980, 11A, 387.
10. K.J. Irvine, F.B. Pickering and T. Gladman: J.I.S.I., 1967, 205, 161.
11. R.W. K. Honeycombe: Scandanavian J. of Met., 1979, 8, 21.
12. K. Narita: Trans. of ISI Japan, 1975, 15, 147.
13. H. Chino and K. Wada: Yawata Technical Report, No. 251, 1965, pp. 75-100.
14. M.J. Crooks, A.J. Garratt-Reed, J.B. Vandersande and W.S. Owen: Met. Trans. A, 1981, 12A, 1999.

15. D.C. Houghton, G.C. Weatherly and J.D. Embury: "Thermomechanical Processing in Microalloyed Austenite",Proceedings, 1982, Met. Soc. AIME, in the press.
16. R.C. Hudd, A. Jones and M.N. Kale: J. of Iron and Steel Institute, 1971, 209, 121.
17. V.K. Lakshmanan: Ph.D. Thesis, McMaster University, 1977.
18. H.J. Goldschmidt:'Interstitial Alloys', 1967, Plenum Press, New York.
19. L.E. Toth: 'Transition Metal Carbides and Nitrides', 1971, Academic Press, New York.
20. E.K. Storms: 'The Refractory Carbides', 1967, Academic Press, New York.
21. T.J. George and J.J. Irani: J. Australian Institute of Metals, 1968, 13, 94.
22. T.J. George and N.F. Kennon: J. Australian Institute of Metals, 1972 17, 73.
23. S. Kanazawa, A. Nakashima, K. Okamoto and K. Kanaya: Trans. ISI Japan, 1976, 16, 486.
24. S. Matsuda and N. Okumura: Trans. ISI Japan, 1978, 18, 198.
25. G. Cliff and G.W. Lorimer: J. of Microscopy, 1975, 103, 203.
26. D.C. Houghton: Electron Microscopical Society of America, 1981, p. 352, Annual Meeting Proceedings.
27. P.G. Shewmon: 'Diffusion in Solids', p. 65, 1963, McGraw-Hill, New York.
28. C.C. Houghton: EMAG 81, p. 245, 1981, Inst. of Physics Proceedings, ed. M.J. Goringe.

Figure Captions

Figure 1. Schematic representation of the time - temperature characteristics during Gleeble weld cycle simulation.

Figure 2. Schematic diagram of submerged arc weld geometry indicating the region of the H.A.Z. investigated by the strip replica technique.

Figure 3. Predicted mole fractions of precipitated carbonitrides as a function of temperature. Three levels of intermixing are shown to demonstrate the increased precipitate yield and solution temperature rise due to inter-solution of binary compounds.

Figure 4. Atom fractions of elements in the complex compound $Ti_xNb_{(1-x)}$ $(C_yN_{(1-y)})_v$, precipitating from austenite over the temperature range (1400 → 900)°C.

Figure 5. (a) CTEM micrograph of "dendritic" precipitates extracted from as-cast heat #5. X13,500.

(b) STEM annular dark field micrograph of a row of contiguous cuboidal precipitates found in heat #5 after annealing at 1200°C for 16 h. X10,000.

(c) STEM bright field micrograph of facetted precipitates extracted from heat #5 after 4 h at 1300°

(d) STEM bright field micrograph of precipitates with orthogonal symmetry found in heat #5 after 4 h at 1400°C.

Figure 6. Vegard's law interpolation to determine approximate $(\frac{N}{C+N})$ ratio in precipitates found in steel #5 as cast and after equilibration anneals at 1200°C, 1300°C and 1400°C. Experimental lattice parameters from CTEM-SAD data, STEM-EDS X-ray measurements provide $(\frac{Ti}{Ti+Nb})$ ratio and lattice constants of $Ti_xNb_{1-x}N$ and $Ti_xNb_{1-x}C$ from Goldschmidt.[18]

Figure 7. STEM EDS X-ray measurements of Ti concentrations in the precipitates extracted from heat #5 after isothermal anneals at 1200°C, 1300°C and 1400°C. The curves are calculated Ti concentrations in the double nitride $Ti_xNb_{1-x}N$ for "available" titanium concentrations of 0.005 w/o and 0.01 w/o.

Figure 8. STEM bright field micrograph of typical controlled-rolled precipitate morphology, heat #5. A similar bimodal size distribution was detected in all Ti bearing heats.

Figure 9. (a) STEM bright field micrograph of a composite precipitate extracted from controlled rolled heat #5.
(b) STEM microdiffraction patterns from the top, centre and bottom regions of the precipitate indicated in (a).
(c) STEM EDS X-ray spectra from the precipitate regions indicated in (a).

Figure 10. (a) STEM bright field micrograph of a typical cluster of precipitates located at a prior austenite grain boundary in the HAZ of SAW plate, heat #5.
(b) STEM EDS X-ray spectrum from external ∿10 nm "skin" of precipitate in (a) showing significant titanium enrichment.
(c) STEM EDS X-ray spectrum from central region of the large precipitate in (a).

Figure 11. Histograms of precipitate size distributions in the actual CGHAZ of SAW plates, taken from heats 2, 3, 4 and 5.

Figure 12. Prior austenite grain size plotted as a function of radial displacement from the fusion boundary through the HAZ for all heats.

List of Tables

Table I Steel Chemical Compositions

Table II Structural Changes Due to Isothermal Annealing

Table III Controlled Rolled Microstructures

Table IV Gleeble Weld Simulation Microstructures

Table I. Steel Chemical Compositions (in w/o)

Heat No.	Aim Ti	Aim N	C	Mn	P	Si	Final Ti	Final N	Ti/N (wt)	Ti/N Atom Ratio
1	-	0.006	0.071	1.97	0.002	0.27	-	0.009	-	-
2	0.010	0.006	0.055	1.96	0.002	0.25	0.011	0.005	2.2	0.65
3	0.020	0.012	0.070	1.91	0.002	0.34	0.033	0.007	4.7	1.4
4	0.020	0.012	0.065	1.81	0.007	0.27	0.011	0.009	1.22	0.36
5	0.040	0.012	0.076	1.98	0.002	0.33	0.039	0.010	3.9	1.15

The Cb level in all steels was between 0.050 to 0.054 w/o.
The Mo level in all steels was between 0.29 and 0.33 w/o.
The S level in all steels was between 0.003 and 0.005 w/o.

Table II. Structural Changes Due to Isothermal Annealing

	As Cast	1100°C	1200°C	1300°C	1400°C	1450°C
Precipitate Morphology	Large feathery "dendrites" several microns in size appear at primary grain boundaries. Few smaller dendrites ∿20 nm	As cast precipitate morphology persists. Insufficient time for equilibration after 16 h.	Anneal time 16 h Considerable size variation 10-500 nm. Stringers along prior austenite grain boundaries	Anneal time 4 h Cuboidal precipitates with orthogonal facets 10 nm-500 nm Rows of precipitates several microns in length	Anneal time 4h Fewer and larger facetted orthogonal particles randomly distributed	No facetted or spheroidal precipitates were detected after 4 h at temperature
Prior austenite grain size (μm)	The heterogeneous microstructure prevented grain size measurement		67±8 1 h 70±10 4 h 70±10 16 h	227±26 1 h 386±40 4 h	444±30 1 h 446±50 4 h	459±40 4 h
STEM Microanalysis	TiN cubes. Niobium rich "dendrites" of constant composition	No analyses performed; chemical heterogeneity suspected.	Annealing for 16 h titanium rich nitride precipitates	After 4 h, only titanium and nitrogen rich precipitates persist	As for 1300°C after 4 h anneal	After 4 h, only MnS and oxide inclusions were found.
$\frac{Ti}{(Ti+Nb)} \times 100$	17±2%		55±6 w/o	73±3 w/o	87±4 w/o	
$\frac{N}{(N+C)} \times 100$	∿100%		∿88 a/o	∿100 a/o	∿89 a/o	
Lattice constant a_o, nm	0.435±0.002		0.432±0.002	0.427±0.002	0.426±0.002	

Table III Controlled Rolled Microstructures

Heat No. -	#1 0.00 w/o Ti	#2 0.011 Ti 0.005 N	#3 0.033 Ti 0.007 N	#4 0.011 Ti 0.009 N	#5 0.039 Ti 0.010 N
Precipitate morphology and distribution	Large size and shape variation. Particles ∿100 nm prolate spheroids fine precipitates approximately spheroidal. Random spatial distribution.	Bimodal size and shape distribution. Precipitates ≳50 nm cuboidal finer precipitates approx. spheroidal.	Precipitates characterized by both size and shape. cuboids ≳50 nm spheroids ≲50 nm several large(μm) TiN particles	Two distinct characteristic precipitate species, cuboids 20 - 200 nm and spheroids ≲ 20 nm mean range ∿10 nm	Well defined cuboid and spheroid population, cuboids of the size range 50-200 nm and spheroids 3-30 nm. Some large TiN particles.
STEM EDS X-ray microanalysis (elemental ratios in w/o)	Only niobium detected in precipitate size range ∿10 nm - 200 nm. Precipitate of general form Nb(C,N)	Cuboids mean edge length 110 nm $\frac{Ti}{Ti+Nb}\cdot 100 = 30$ Probably(Ti,Nb)N Spheroids ∿20 nm contain only Nb. Probably Nb(C,N)	Cuboids 100-200 nm $\frac{Ti\cdot 100}{Ti+Nb} = 66\pm3$ 50-100 nm $\frac{Ti}{Ti+Nb} = 48\pm6$ probably(Ti,Nb)N Spheroids size range 2-50 nm niobium rich some Mo,Ti (Nb,Mo,Ti)CN	Cuboids 20-50 nm $\frac{Ti\cdot 100}{Ti+Nb}=31\pm4$ 75-299nm $\frac{Ti\cdot 100}{Ti+Nb}=69\pm4$ probably(Ti,Nb)N Spheroids Fine dispersion ≲20 nm, niobium rich some Mo probably Nb(C,N)	Cuboids $\frac{Ti}{Ti+Nb}\cdot 100 = 61\pm7$ (Ti,Nb) N Spheroids niobium rich with $\frac{Ti\cdot 100}{Ti+Nb} \sim 12$ some Mo in ppts ≲ 20 nm(Nb,Mo,Ti)CN
Presence of Mo, Mn, Al, Fe in precipitates	None	None	Mo detected	None	Mo detected

Table IV. Gleeble Weld Simulation Microstructures

Heat No. -	#1 0.00 w/o Ti	#2 0.011 w/o Ti 0.005 w/o N	#5 0.039 w/o Ti 0.010 w/o N
Precipitate characterization	No detectable precipitates	No spheroids. Random distribution of well define cuboidal geometry. No composite particles.	No spheroids. Clusters and rows of facetted cuboids. No evidence of 'cored' particles.
Size range nm	-	30 - 100	20 - 150
Mean size nm	-	∿50	∿52
$\frac{Ti}{(Ti+Nb)}$ x100 w/o	-	60 ± 6	56 ± 6
Prior austenite grain size, μm	100	64	66

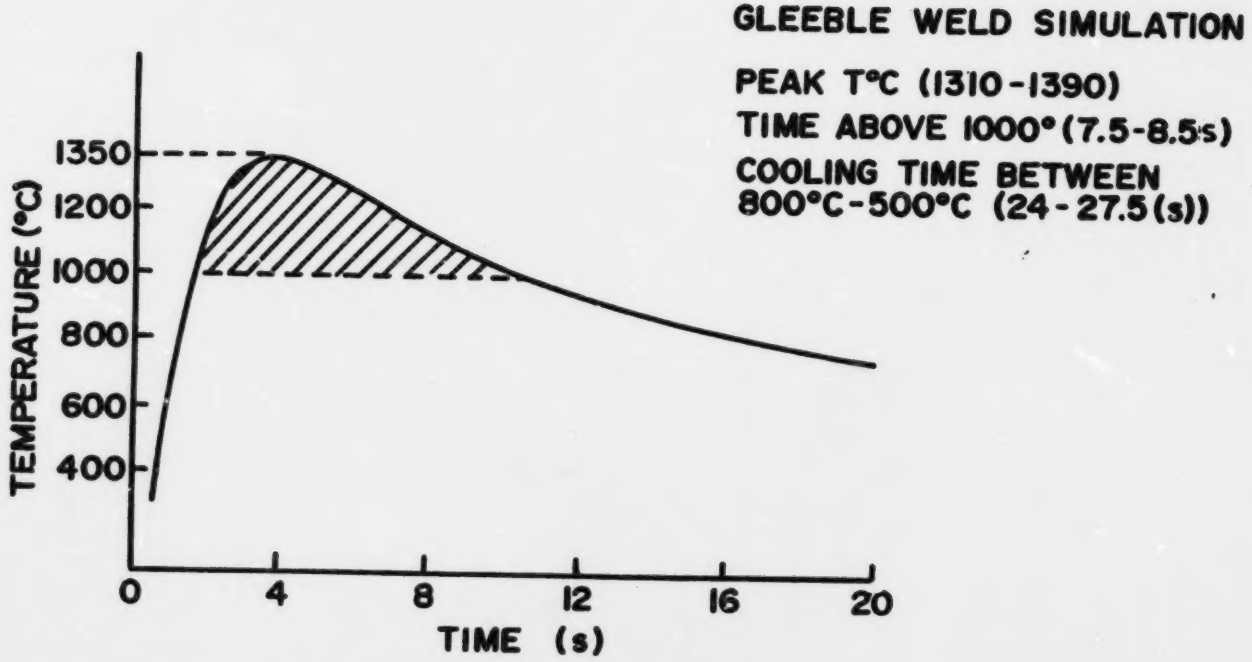

Figure 1. Schematic representation of the time - temperature characteristics during Gleeble weld cycle simulation.

Fig 1

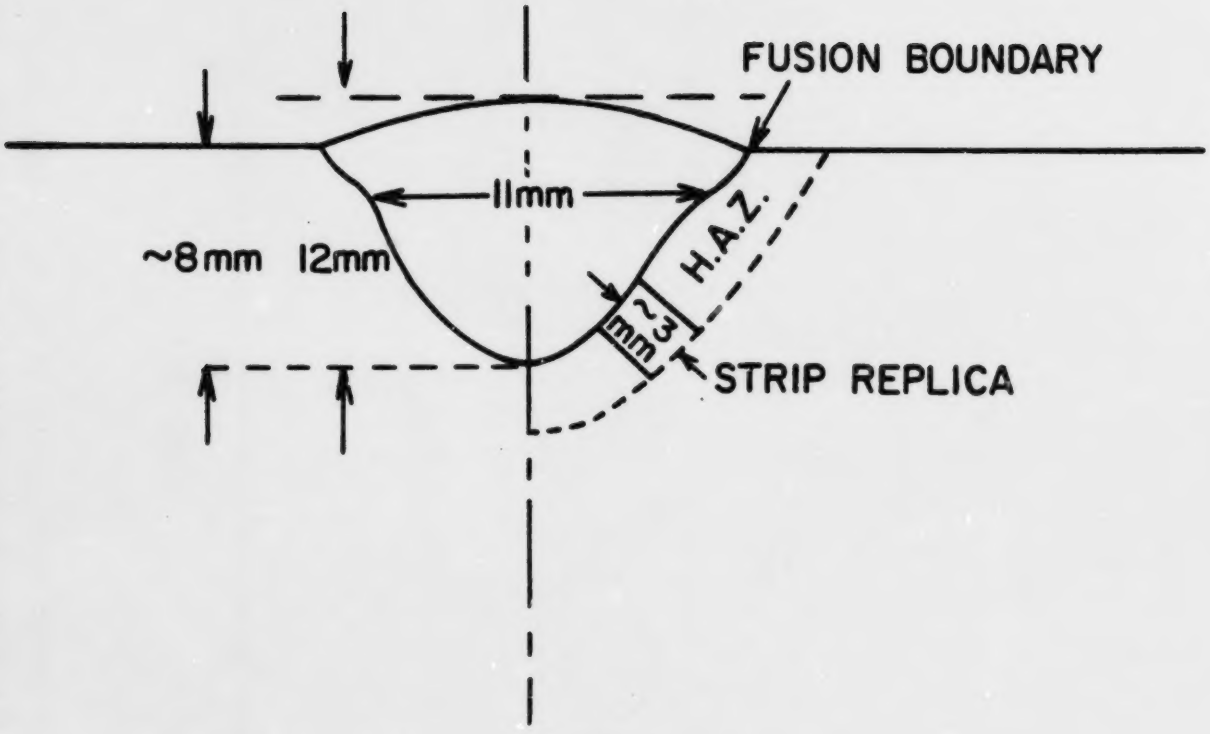

Figure 2. Schematic diagram of submerged arc weld geometry indicating the region of the H.A.Z. investigated by the strip replica technique.

Figure 3. Predicted mole fractions of precipitated carbonitrides as a function of temperature. Three levels of intermixing are shown to demonstrate the increased precipitate yield and solution temperature rise due to inter-solution of binary compounds.

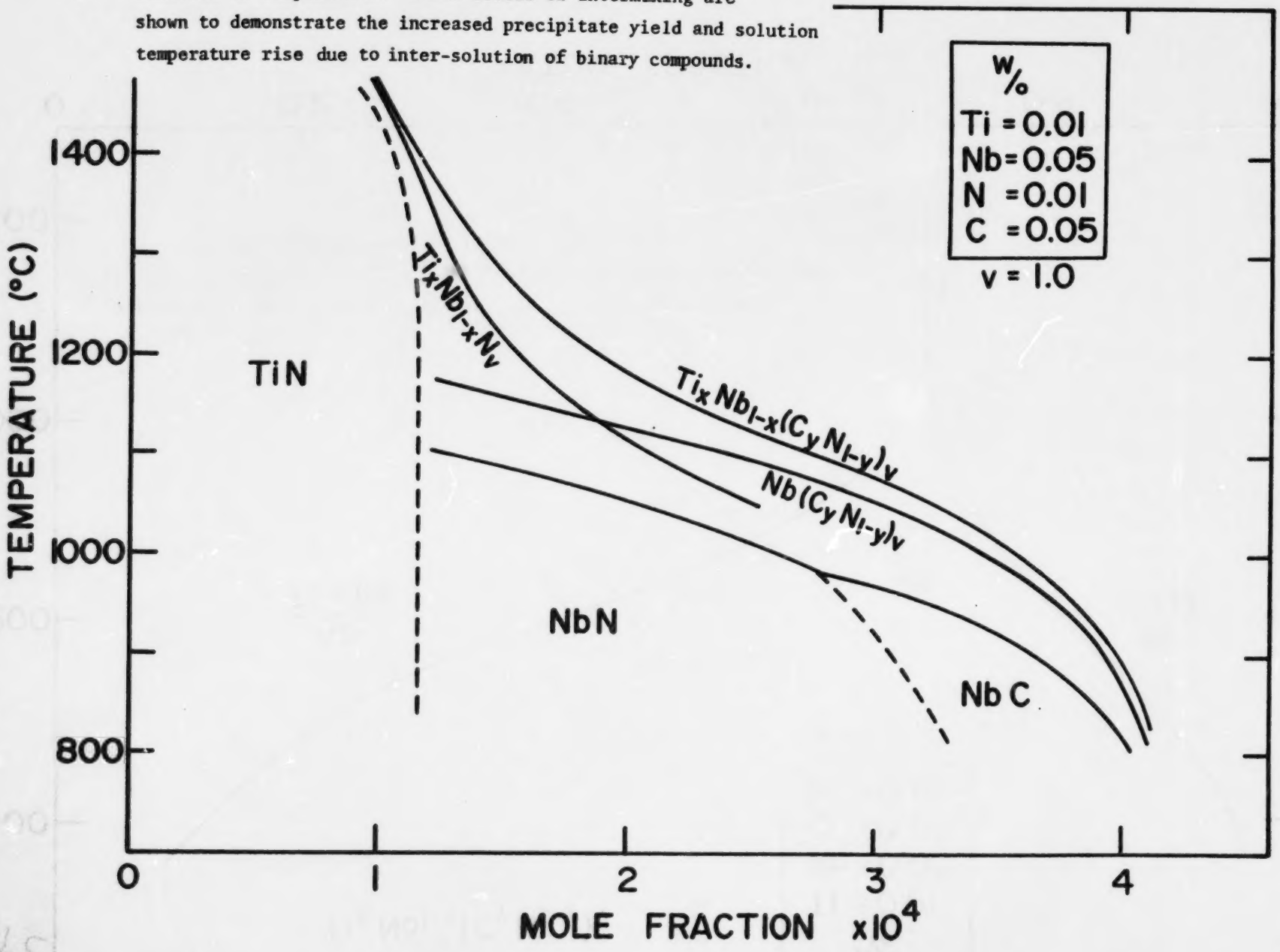

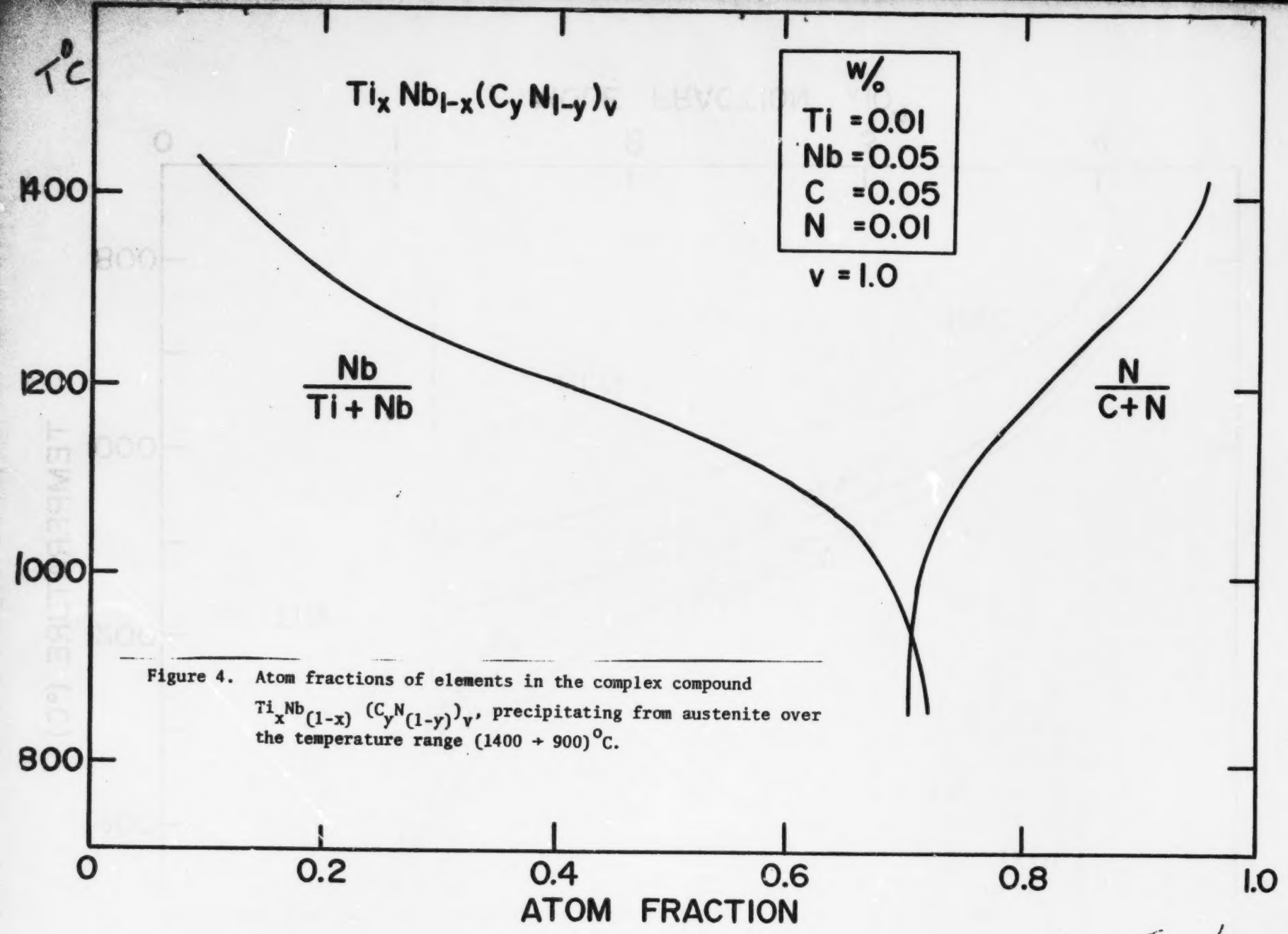

Figure 4. Atom fractions of elements in the complex compound $Ti_x Nb_{(1-x)} (C_y N_{(1-y)})_v$, precipitating from austenite over the temperature range (1400 → 900) °C.

Fig 4

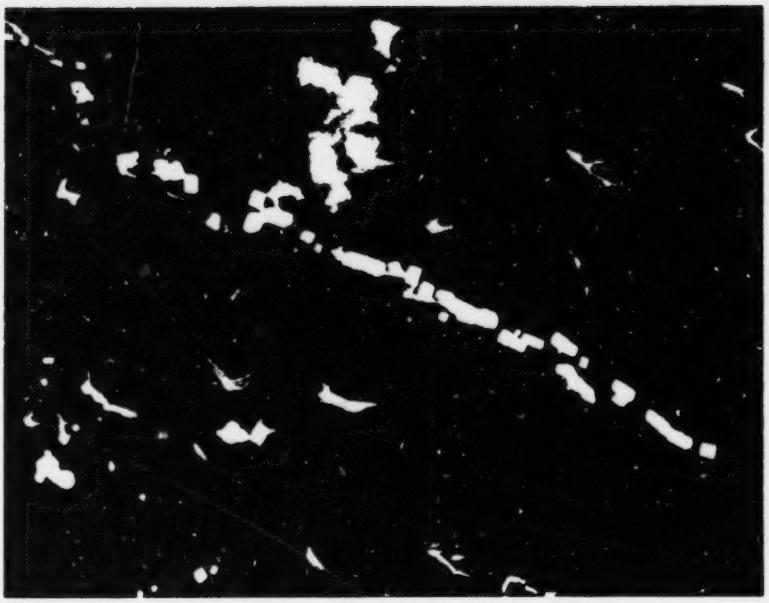

5(b)

5(c)

Figure 5. (a) CTEM micrograph of "dendritic" precipitates extracted from as-cast heat #5. X13,500.

(b) STEM annular dark field micrograph of a row of contiguous cuboidal precipitates found in heat #5 after annealing at 1200°C for 16 h. X10,000.

(c) STEM bright field micrograph of facetted precipitates extracted from heat #5 after 4 h at 1300°

(d) STEM bright field micrograph of precipitates with orthogonal symmetry found in heat #5 after 4 h at 1400°C.

Fig 5(a)

Fig 5(d)

Figure 6. Vegard's law interpolation to determine approximate $(\frac{N}{C+N})$ ratio in precipitates found in steel #5 as cast and after equilibration anneals at 1200°C, 1300°C and 1400°C. Experimental lattice parameters from CTEM-SAD data, STEM-EDS X-ray measurements provide $(\frac{Ti}{Ti+Nb})$ ratio and lattice constants of $Ti_xNb_{1-x}N$ and $Ti_xNb_{1-x}C$ from Goldschmidt.[18]

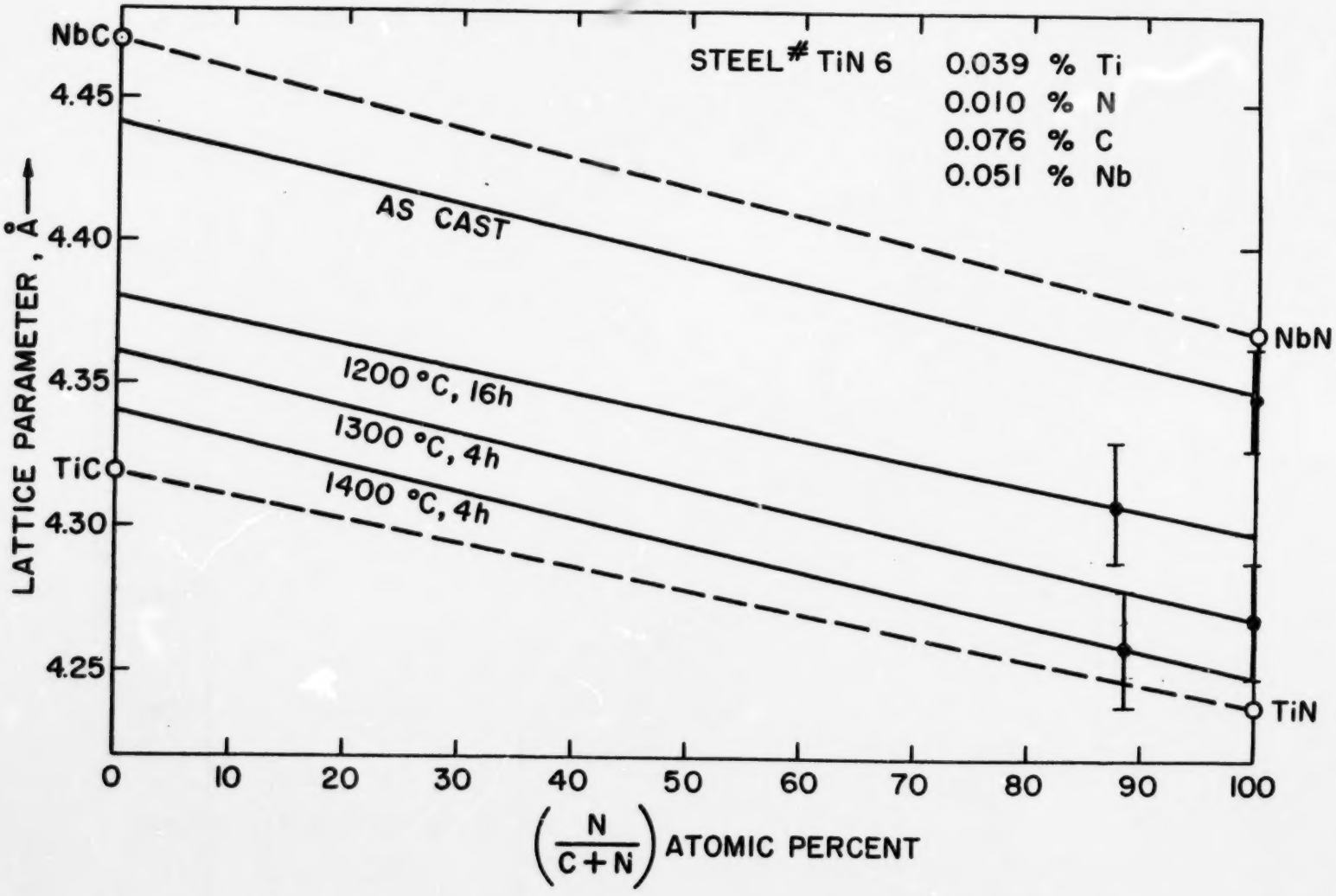

Figure 7. STEM EDS X-ray measurements of Ti concentrations in the precipitates extracted from heat #5 after isothermal anneals at 1200°C, 1300°C and 1400°C. The curves are calculated Ti concentrations in the double nitride $Ti_xNb_{1-x}N$ for "available" titanium concentrations of 0.005 w/o and 0.01 w/o.

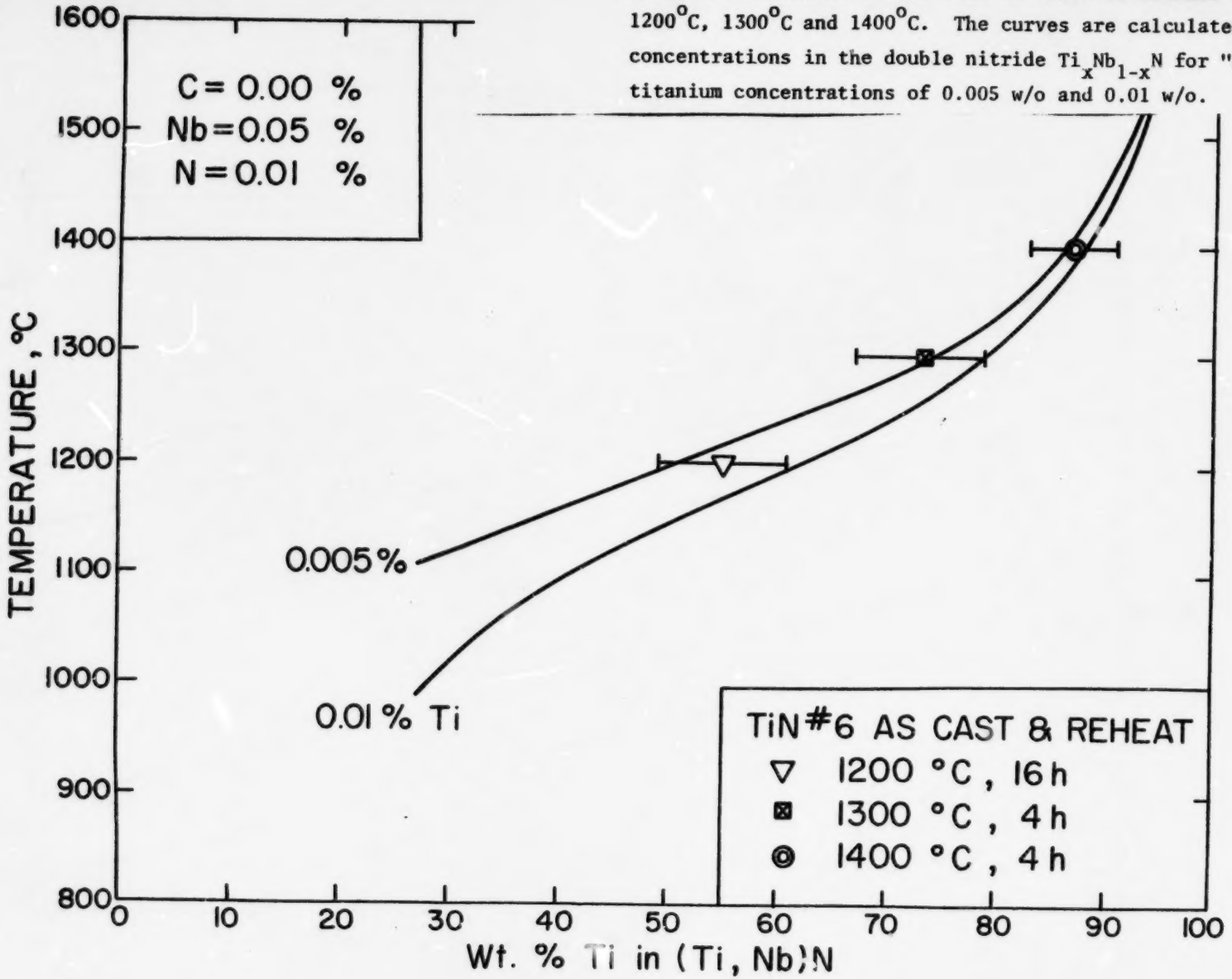

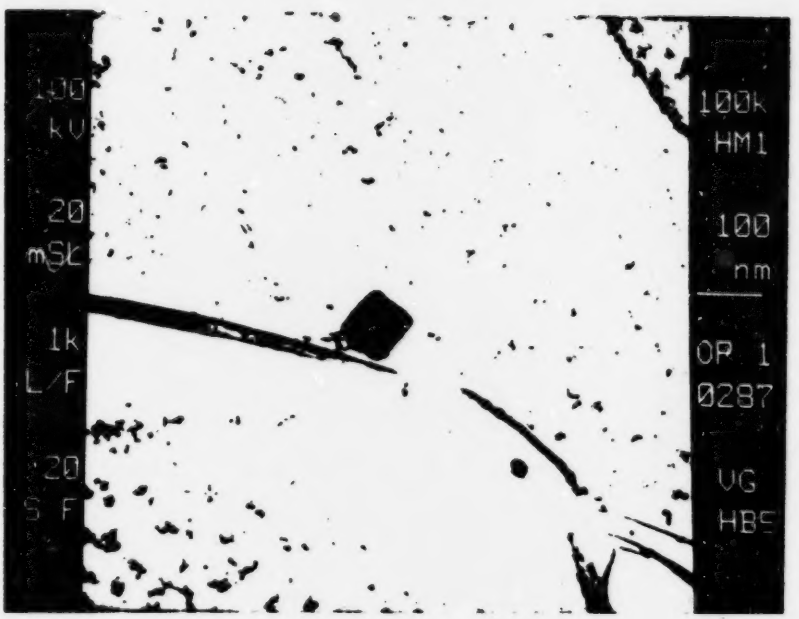

Figure 8. STEM bright field micrograph of typical controlled-rolled precipitate morphology, heat #5. A similar bimodal size distribution was detected in all Ti bearing heats.

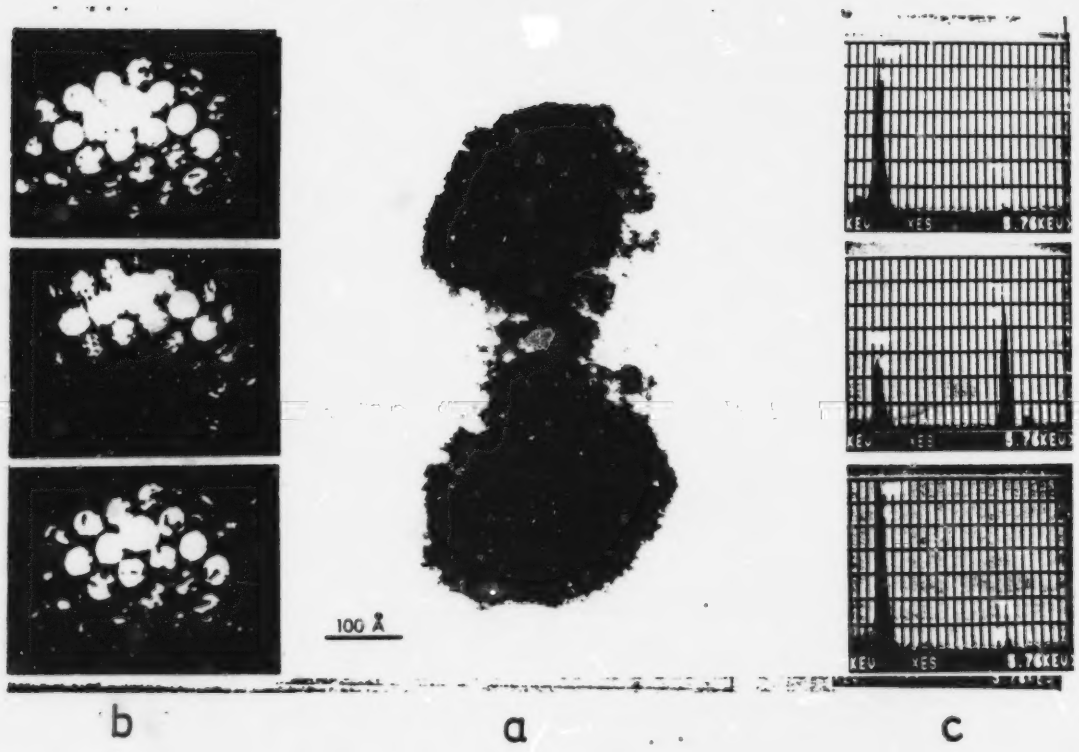

Figure 9. (a) STEM bright field micrograph of a composite precipitate extracted from controlled rolled heat #5.
(b) STEM microdiffraction patterns from the top, centre and bottom regions of the precipitate indicated in (a).
(c) STEM EDS X-ray spectra from the precipitate regions indicated in (a).

10 a)

Figure 10. (a) STEM bright field micrograph of a typical cluster of precipitates located at a prior austenite grain boundary in the HAZ of SAW plate, heat #5.
(b) STEM EDS X-ray spectrum from external ~10 nm "skin" of precipitate in (a) showing significant titanium enrichment.
(c) STEM EDS X-ray spectrum from central region of the large precipitate in (a).

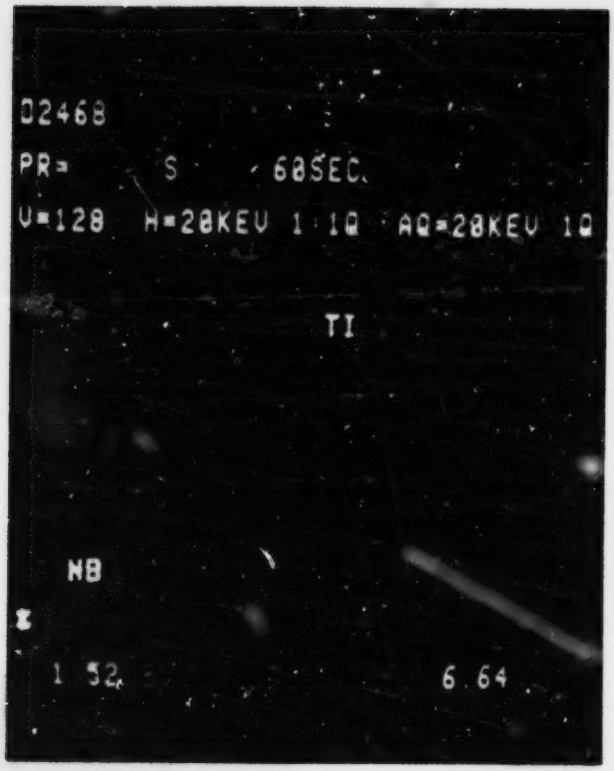

Fig 10(b)

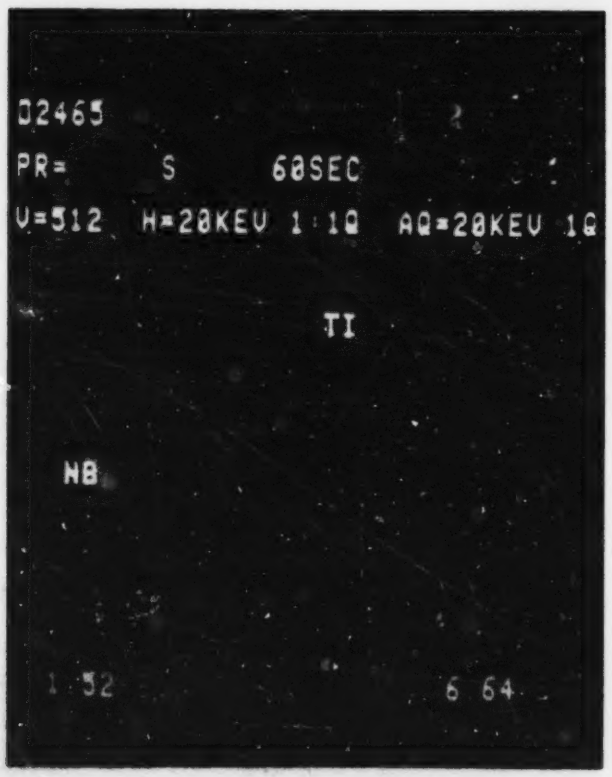

Fig 10(c)

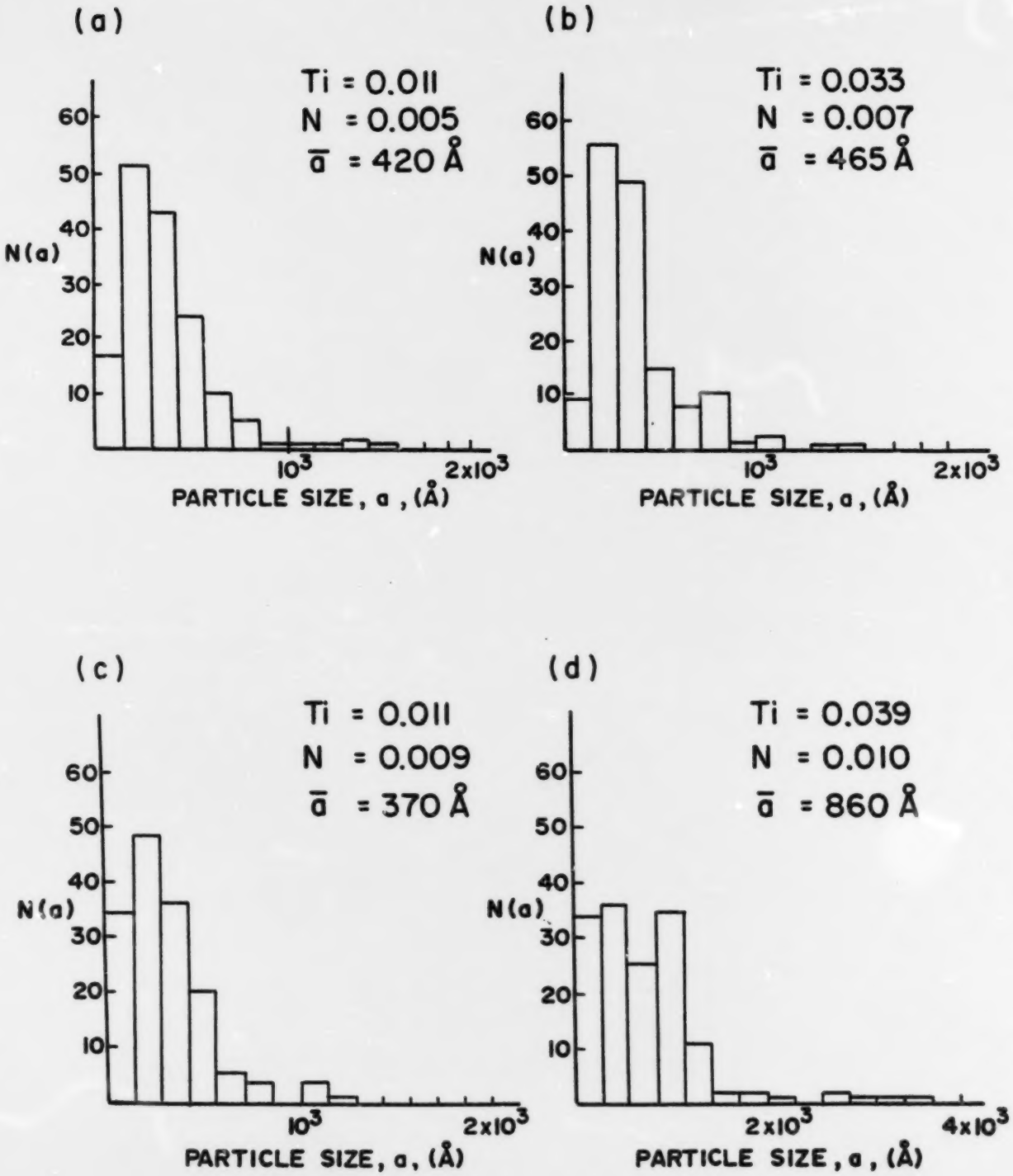

Figure 11. Histograms of precipitate size distributions in the actual CGHAZ of SAW plates, taken from heats 2, 3, 4 and 5.

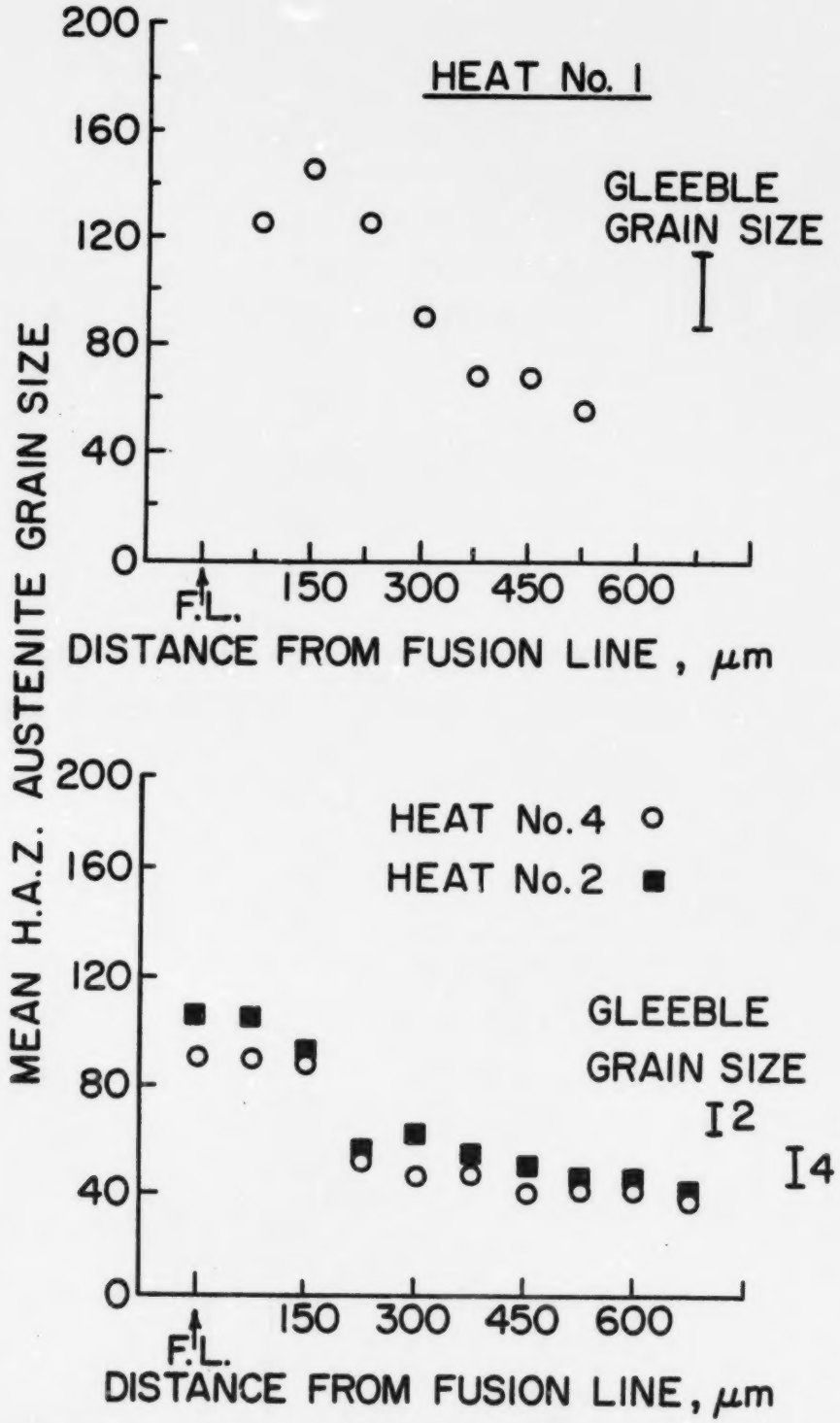

Figure 12 Prior austenite grain sizes plotted as a function of distance from the fusion line for the heat affected zones of various heats.

Number/
Numéro

Scanning Transmission Electron Microscopy of Microalloyed Steels

by

J.D. Embury and G.C. Weatherly

Final Report to CANMET

SCANNING TRANSMISSION ELECTRON MICROSCOPY OF MICROALLOYED STEELS

FINAL REPORT

BY

J.D.Embury and G.C.Weatherly

Work on this project was conducted under the auspices of
Physical Metallurgy Research Laboratories
Canada Centre for Mineral and Energy Technology
Energy, Mines and Resources Canada

DSS FILE NO.	:	03SU.23440-0-9133
DSS CONTRACT SERIAL NO.	:	OSU81-00230
CANMET PROJECT NO.	:	425101
CANMET SCIENTIFIC AUTHORITIES:		Drs.J.D.Boyd and T.Malis

June 1984

This report should be cited by D.S.S. File No.
03SU.23440-0-9133

Scanning Electron Microscopy of Microalloyed Steels

Introduction

The research contract had two basic objectives: a) to increase the detailed understanding of the behaviour of microalloying elements in H.S.L.A. steels, and b) to explore the potential value of the Scanning Transmission Electron Microscope (S.T.E.M.) to problems in physical metallurgy.

In order to meet these objectives a variety of studies have been undertaken using both microalloyed steels and other materials. Some aspects of these studies are relatively complete and have been written up for publication. These are included in this report in the form of appendices. In the course of the work some new experimental techniques were developed and where appropriate these are described in detail.

In approaching the application of quantitative electron microscopy to microalloyed steels a comprehensive approach was elected. This approach was premised on the need to relate the studies to current production methods and to attempt to delineate the evolution of the final microstructure. Thus attention has been given to the analysis of the initial cost structure of continuously cast materials and materials prepared by laboratory simulations of continuously cast materials. This is a difficult problem involving the development of a range of overlapping experimental methods in order to examine both the scale of the microstructure and the detailed composition of precipitates simultaneously.

The interpretation of the resulting structures had demanded the development of a new model of microsegregation for which the authors are most grateful for the contributions made by Dr. Subramanian.

In attempting to explore the potential of the S.T.E.M. in problems of physical metallurgy it was decided to consider some problems in which S.T.E.M. could provide data which is complementary to other high resolution analytical techniques such as scanning auger spectroscopy. This method was applied to the analysis of phosphorous segregation in temper embrittled steels and involved the preparation of various standards for S.T.E.M. analysis.

One feature of the S.T.E.M. analysis which has not so far met with a great deal of success is the electron loss spectroscopy method for analyses of light elements. In part the difficulties have arisen due to the design of the V.G. HB5. However, it appears that this method will be difficult to apply in a quantitative manner although with the assembly of a library of standard spectra some useful analysis may be possible.

In order to give a comprehensive coverage to the various aspects of the S.T.E.M. work which has been performed, separation sections will be devoted to each technique. A large number of researchers have been involved and they are acknowledged in the authorship of the various sections.

Section A

Use of Analytical Electron Microscopy to Study Intergranular Carbides and Phosphorus Segregation in Cr-Mo-V Steels

(This portion of the report contains work performed by J.L. Verger-Gaugry, T. Castillo and C. Hyatt.)

Introduction

Segregations of residual elements such as P, Sn, Sb, As in grain boundaries are considered to be the major cause of temper embrittlement and creep embrittlement of steels (1). An attempt to correlate the creep embrittlement and temper embrittlement which are induced by P in a 3/2 Cr-2/3 Mo-1/3V steel (steel 0, table 1), was performed on materials previously aged at temperatures ranging from 500 to 600°C (2,3). The characterization of the chemistry in the region of the prior austenite boundaries by Auger electron spectroscopy (AES) was difficult to interpret directly from the P Auger signal. The compositions of the steels used in the study are summarized in Table 1. In steels P_1 and P_2 increase of the intergranular concentration of P was observed at 550°C and 600°C by Auger spectroscopy; however, this may correspond either to an actual increase in the segregation of phosphorus in grain-boundaries, or to an artifact in the measurement due to the Auger spectroscopy techniques. This artifact can arise because the primary beam, in the spectrometer, provides a composition of the fracture surface averaged on the whole area sampled by the beam. In this respect, three

phenomena can relate to the P signal measured in grain-boundaries and can be summarized as follows:

a) Phosphorus, when segregating to prior austenitic boundaries, has been shown to accelerate the nucleation of cavities and decrease their growth rate (2,3,4). The dimension of the cavities is usually smaller than the spot size of the incident beam in the Auger spectrometer, and does not permit the observer to differentiate between P in the altered parts of boundaries and the inner surfaces of cavities. In this case, the measured intergranular concentration of P is not specific to the grain-boundaries or cavity free surfaces but takes an intermediate value between the segregation characteristic of these two interfaces.

b) Under stress, the sequence of precipitation is accelerated and the formation of carbides which are associated with a positive volume change (5) e.g.: Mo-rich carbides form more easily than Cr-rich or V-rich carbides. The precipitation of Mo-rich carbides in prior austenitic boundaries has been studied by AES up to the disappearance of the free Mo, and occurs faster at 600°C than at 550°C (Fig. 3), in P_1 as in P_2. Due to the scavenging effect of Mo on P in the bulk material (6,7,8), the precipitation of Mo induces a release of all the phosphorus trapped in (Mo,Fe)-phosphides in the matrix, leading to a greater amount of free phosphorus and hence an increase of its segregation. Such an increase is expected to be small in the steels (P_1,P_2) which are strongly enriched in phosphorus but may be more apparent in commercial or synthetic steels containing smaller P contents (8,9).

c) The Mo-rich carbides, are known to contain significant concentrations of P (10,11). Thus as Mo has been shown to precipitate in prior austenitic boundaries in steels P_1 and P_2, we can expect a contribution of those Mo-rich carbides formed during creep and eventually of other carbides, to the P signal in A.E.S. This contribution must be subtracted from the P (A.E.S.) signal with respect to the percentage of the surface carbides occupied in grain-boundaries.

Thus, the purpose of the present work was to investigate the possible causes of the increase of the intergranular concentration of P from an initial equilibrium value in steels P_1 and P_2. The method consisted of using carbon extraction replica techniques and X-ray microanalysis in a V.G. HB5 Scanning Transmission Electron Microscope (S.T.E.M.) to study the composition and morphology of carbide precipitates. In addition, using a high resolution Auger electron spectrometer with a spot size of the order of a few tenths of a micron to characterize the difference between the equilibrium segregation of P in grain boundaries and on the inner surfaces of cavities.

Experimental

Three laboratory steels with carbon contents in the range .22 - .24 were produced from electrolytic iron at Imply*, the reference steel, steel 0, having the basic composition 3/2 Cr - 2/3 Mo - 1/3 V (Table 1), the steels designated $\underline{P_1}$ and $\underline{P_2}$ were enriched in phosphorus, to 290 ppm and 650 ppm respectively. These steels were austenized at 1050°C, 1 h, quenched (Fig. 1)

---

*Centre de Recherche Creusot-Loire d'Imphy, France.

and tempered at 700°C, 4 hrs., WQ to give a microstructure composed of tempered martensite with approximately 15% bainite. Creep tests were then performed for each steel, up to fracture, at 500°C using a stress of 350 MPa, at 550°C at a stress of 250 MPa and 600°C using stresses of 250, 200 and 150 MPa. Additional creep tests on these steels were interrupted after 500 and 1000 hours at 500°C and 550°C. Annealing treatments without stress were also carried out on these steels at 500°C, 550°C, 600°C with aging times ranging from 1 to 3000 hours.

Circumferential notches were machined in some creep test specimens and in some test specimens which had been annealed without stress, and were broken in-situ at -100°C when 10^{-10} torr in a RIBER Scanning Auger Electron Spectrometer equipped with a cylindrical mirror analyzer (CMA), and a coaxial electron gun, using a 3 or 5 kV, 4 μA primary beam and a peak to peak modulation voltage of 2V. The incident beam allowed spot sizes of 5 to 20 μm.

Argon ion sputtering of the fracture surfaces was used to determine whether a particular element was segregated or precipitated in the grain-boundaries. If only in a segregated form, its Auger signal is removed within less than a minute using a 2 keV, 50 $\mu A.cm^{-2}$ beam, while if the element is in the form of a precipitate, it remains almost constant for hours of ion bombardment. If V, Cr appear totally precipitated, the evolution with depth of the Mo Auger signal often indicates an intermediate situation between a pure segregation, as for P, and a complete precipitation, as for V, and has been interpreted previously (2,3,8). Calculations of

concentrations from the peak to peak heights on the differentiated spectra was performed as described previously (8).

Polished cross-sections of specimens were etched in a 5% nital solution and coated with a 1000-3000 A thick C-film by evaporation under vacuum. The separation of the C-replica from the etched surface was achieved in distilled water and parts of the film were positioned on copper grids.

X-ray microanalysis was performed under a pressure of 10^{-9} torr in a STEM-HB5 (equipped with an energy dispersive spectrometer) and using an accelerating voltage of 100 kV. Absorption corrections, when necessary, were performed using a common method described by Lorimer (12,13). The k_{MoP} Cliff-Lorimer constant, used in thin film approximation, was determined experimentally as being 4.1 ± .4 from 99% pure $Al_2(MoO_4)_3$ and $AlPO_4$ powders: each of these powders was mixed with liquid epoxy and the resulting suspension was centrifugated to concentrate all the powder near one end of a cylindrical rod of epoxy. This epoxy was hardened and sectioned using an ultramicrotome to give sections ∿700 Å thick. These sections were coated with a ∿50 to 100 Å thick C-film to avoid charging problems in the STEM (14).

MoO_3 powders imbedded in a C-film were used to give a reference background for the X-ray peaks of Mo, especially LL-LN peaks which overlap with the K-peaks of P. The contribution of Mo in the K peaks of P was each time subtracted to give the real contribution of P, which allows determination of the average concentration of P in the volume element crossed by the electron beam.

A second Auger analysis was conducted using a Perkin-Elmer, PH1600 Scanning Auger Multiprobe. Samples were broken in-situ at -80°C, under 5×10^{-10} ton, and analyzed with a 5 kV, .15 μA incident beam using a spot size of .8 μm. Images were formed at lower currents with smaller spot sizes, typically .055 μm and .5 μm, respectively. Differentiated spectra were obtained numerically by a seven points quadratic least squares fit of the spectra followed by a five points quadratic least squares differentiation.

Results and Discussion

a. STEM Microanalysis of Carbides

Since the study of the presence of phosphorous within carbides constitutes the main goal of this investigation, emphasis was placed on the compositional rather than structural analysis. The study was concentrated on creep test specimens of steel P_2, which were fractured during creep at 600°C, under 150 MPa (A), and at 550°C, under 250 MPa (B), for which the largest effects are expected since, on one hand the intergranular and bulk precipitation of Mo was observed to be almost or totally complete in these states (Fig. 2), and in addition an increase in the intergranular P concentration was measured, especially after creep at 600°C, 150 MPa.

All analyzed carbides indicated some enrichment in one or several of the alloying elements (Fig. 3 and 4). In the two states considered (A and B), carbides can be classified according to their composition as follows:

i) Type a, Fig. 3a and 5, is a Mo-V rich carbide and is often found in the matrix, as well as on subgrains or prior austenite boundaries. The diameter of these particles varied from 20 nm in the matrix, to a few hundred nm in the grain-boundaries. They contain Fe, and some Cr. The P/Mo X-ray intensities ratio was always small, of the order of 0.1, and corresponds to a CP/CMo weight concentration ratio of approximately .025 indicating that P is therefore almost absent from this type of carbide. These carbides appear to correspond to V_4C_3 carbides (15) for which some solubility of Mo was reported (16).

ii) Type b, Fig. 3b and 5, is a Cr-Fe rich carbide, possibly M_6C_3 (1), which can contain large amounts of Fe, small quantities of Mo and V, and possibly Mn. The phosphorus content remains small in these carbides, for which CP/CMo reaches $\sim$0.54. Type a and b carbides are by far the most common in these steels.

iii) Type c, Fig. 4a, is a Mo-rich carbide which was only detected in prior austenite boundaries. Microdiffraction patterns obtained on these carbides (Fig. 7) represent sections of a F.C.C. type Bravais lattice, which may be that of M_2C carbides, which are known to be strongly enriched in Mo, and to contain other elements, Cr, V, Fe in small quantities. They contain a small amount of P, and the maximum C_p/CMo ratio observed was $\sim$.02.

iv) Type d, Fig. 4b, is a Fe-rich carbide containing small amounts of Mo, V, Cr, possibly M_3C (15). The P/Fe X-ray intensities ratio never exceeds .008 indicating also that the concentration of P in this type of carbide is very small.

The first three carbides described above were sometimes observed to be enriched in Fe, but at present it is not known whether this is an artifact of the extraction process. Several analyses were performed across precipitates at very high magnification (2×10^6), especially close to the edges, and did not exhibit any increase in the concentration of P. It is probable that the Fe signal arises from the fact that there is some solubility of this element in M_7C_3, V_4C_3 and Mo-rich carbides (16).

Small peaks of Al and Si (Fig. 3 and 4) are visible for almost all carbides, but as in the case of phosphorus, these quantities are too small to allow the determination of the accurate location of these species inside particles by characterizing the composition gradients.

b. AES on Creep Cavities

Auger spectrometry was performed on material heat treated state B, to determine the different degrees of segregation of P in prior austenite grain-boundaries and the inner surfaces of creep cavities in P_2 after creep at 600°C. Due to the small spot size diameter, $\phi \sim .8$ µm, several measurements inside cavities as well as on the planar surfaces of the adjacent boundary were carried out (Fig. 8). The results reveal an enrichment of P inside cavities, at least up to 7 at %, by comparison with the uncavitated part of the boundary. The segregation obtained in this grain-boundary, ~22.6 at %, is close to and slightly below the equilibrium value previously found in this steel for annealing treatments at 600°C, which was determined as being ~26 at %. These two values are in very good agreement in the sense that

segregations differ slightly from one facet to another and that the equilibrium value that we consider is always the maximum segregation observed. This indicates, on one hand, that the precipitation of Mo does not induce any observable increase in the segregation of P in prior austenitic grain-boundaries, as expected, and, on the other hand, that the contribution of intergranular carbides to the P signal is also very weak. Indeed, C-replicas exhibit a very high density of carbides of various sizes in prior austenitic grain-boundaries and most certainly, a certain number of them are intercepted by the incident beam during analysis.

Steel	C	Si	Mn	S	$P_{(ppm)}$	Ni	Cr	Mo	V	$Sn_{(ppm)}$	Aℓ	Cu
0	.243	.27	.76	.0040	70	.19	1.50	.67	.29	9	.048	0.10
P_1	.222	.27	.76	.0034	290	.19	1.49	.68	.29	18	.047	.010
P_2	.236	.27	.76	.C038	650	.19	1.49	.68	.29	14	.061	.011

TABLE 1 - Chemical Composition of Steels (Weight %)

BIBLIOGRAPHY

1. M. GUTTMANN, D. McLEAN in "Interfacial Segregations", ASM, (1979), Metals Park, Ohio; Ed. W.C. JOHNSON, M.J. BLAKELY, 261-348.

2. J.-L. VERGER-GAUGRY, these Docteur-Ingénieur, ENS Mines de Paris, Corbeil, FRANCE.

3. J.-L. VERGER-GAUGRY, M. GUTTMANN in preparation.

4. K.A. ABIKO, R.L. BODNAR, D.P. POPE in "Ductility and Toughness Considerations in Elevated Temperature Service", Ed. Smith, G.V., ASME, (1978), 1-10.

5. B.A. BILBY, F.B. PICKERING, ISI Special Report 64, (1959), 313-318.

6. J. YU, C.J. McMAHON Jr., Met. Trans. A, 11A, (1980), 277-290.

7. C.J. McMAHON Jr., A.K. CIANELLI, H.C. FENG, Met. Trans. A, 8A, (1977), 1055.

8. Ph. DUMOULIN et al., Met. Sci. 14 (1980), 1-15.

9. Ph. DUMOULIN, M. GUTTMANN, Mat. Sci. Engng. 42, (1980), 249-263.

10. A.B. MUHAMMAD, Z.C. SZKOPIAK, Inst. Phys. Conf. Ser. no. 61, Chapter 5, EMAG, Cambridge, (7-10 Sept. 81), 243-244.

11. P. DOIG, D. LONSDALE, P.E.J. FLEWITT, Met. Sci. 16, (1982), 335-344.

12. G.W. LORIMER, Inst. Phys. Conf. Ser. no. 61, Chapter 4, EMAG, Cambridge, (7-10 Sept. 81), 147-152.

13. B.W. ROBERTSON, Ph.D. Thesis, The University, Glasgow, SCOTLAND, 1979.

14. C. HYATT, McMaster University, Hamilton, Ont. Canada, "private communication".

15. R. SMITH, ISI Special Report 64 (1959), 307-311.

16. J.H. WOODHEAD, A.G. QUARRELL, JISI, (June 1965), 605-620.

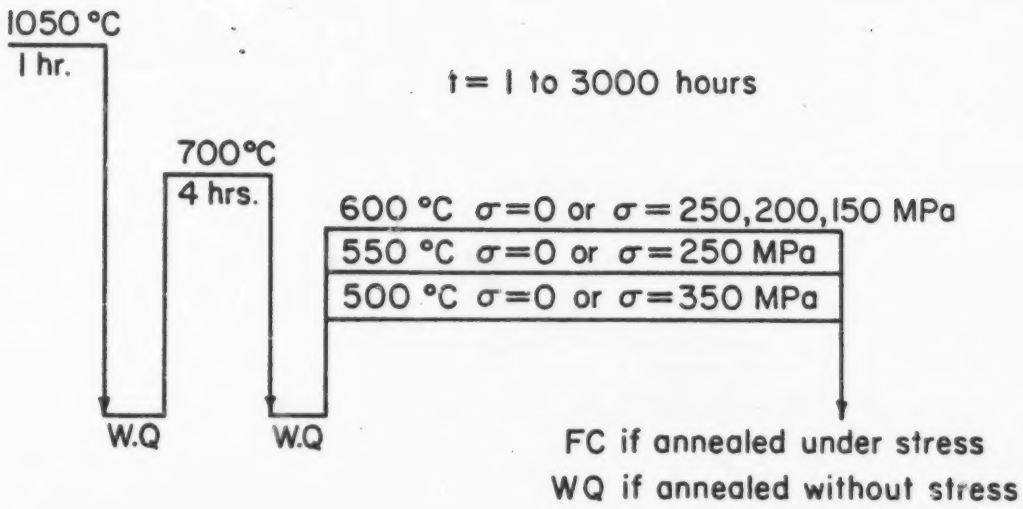

Fig. 1 Heat treatment parameters and loads applied for creep and annealing treatments without stress.

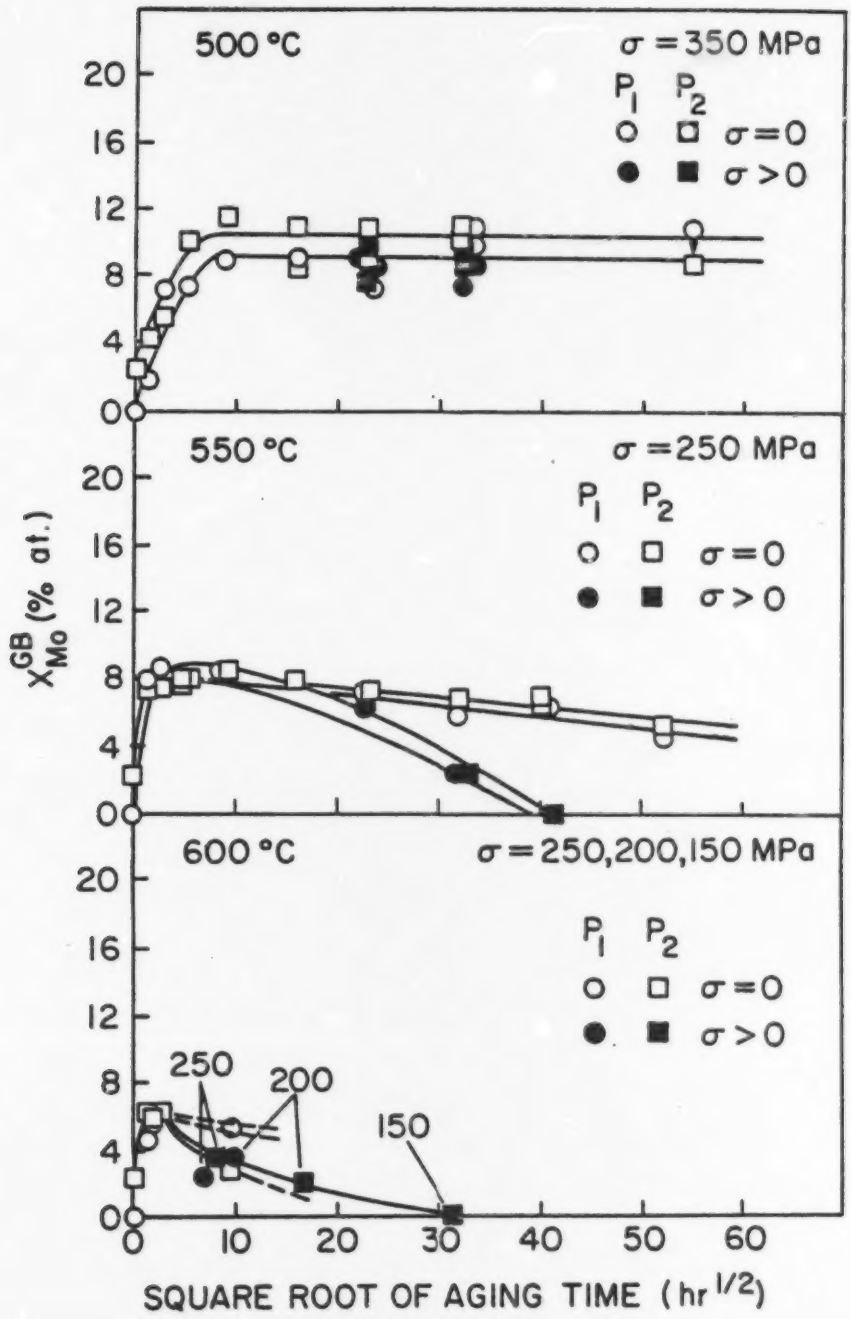

Fig. 2 Evolution of the segregation of Mo in P_1 and P_2 with annealing time, without stress and under stress, at 500, 550, 600°C.

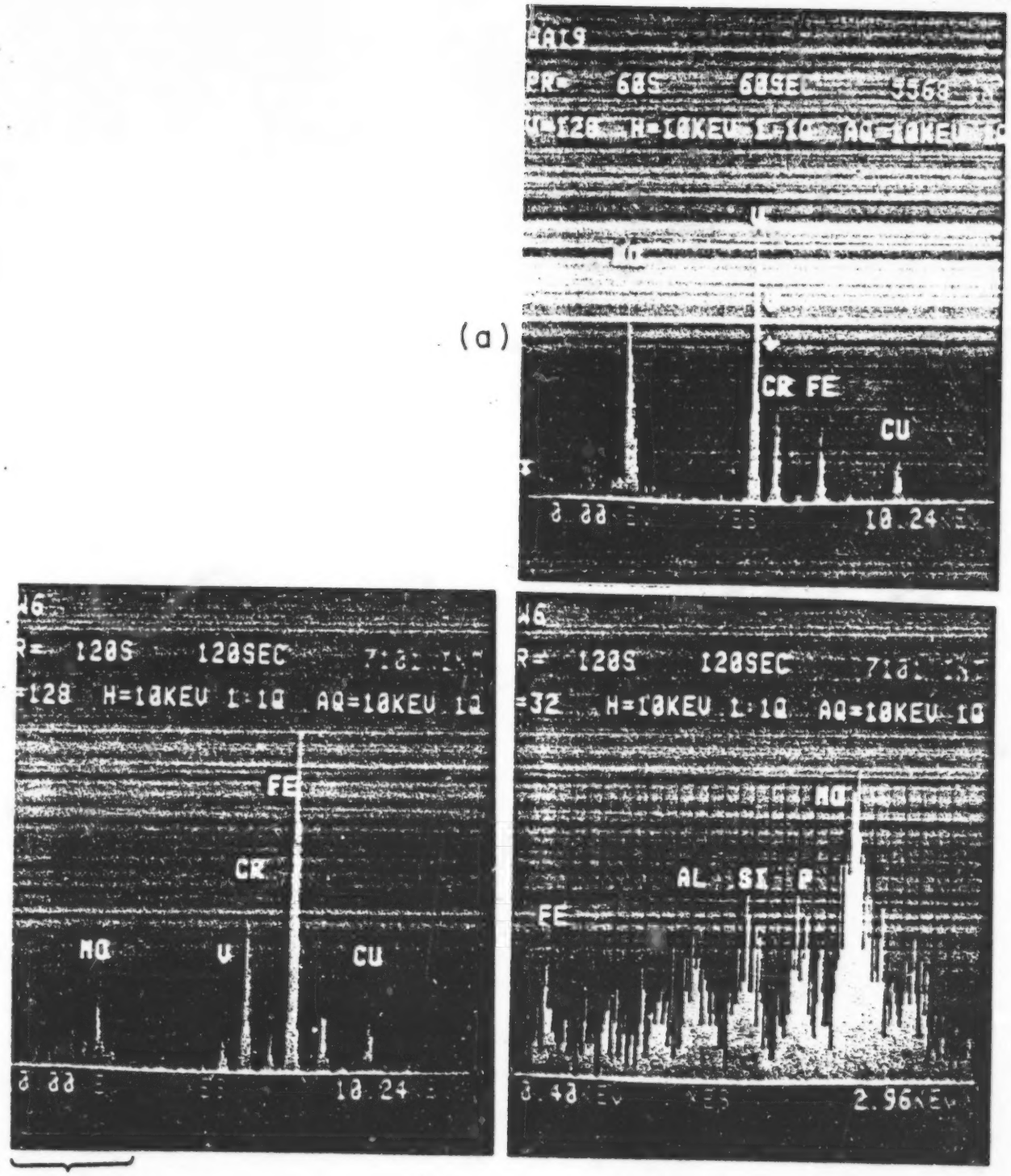

Fig. 3 Carbides, type A and B, in P_2 after creep at 550°C, 250MPa, t_R = 1612 hours or at 600°C, 150 MPa, t_R = 777 hours.

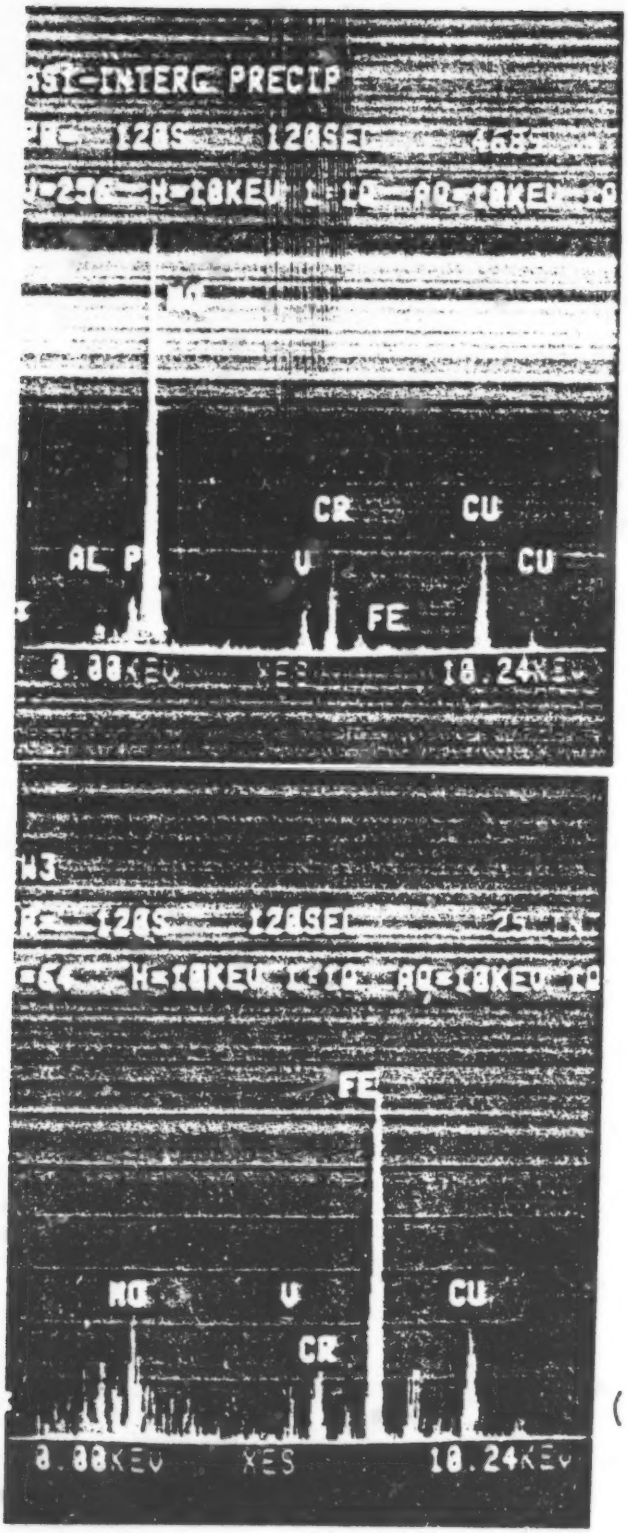

Fig. 4 Carbides, type C and D, in P_2 after creep at 550°C, 250 MPa, t_R = 1612 hours or at 600°C, 150 MPa, t_R = 777 hrs.

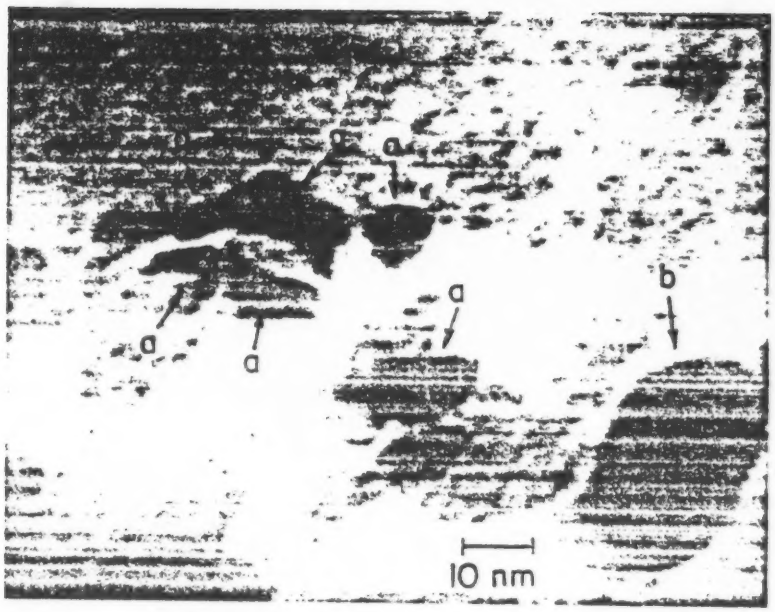

Fig. 5 Bright field image of type A and B carbides in P_2, after creep at 550°C, under 250 MPa, up to rupture, t_R = 1612 hrs.

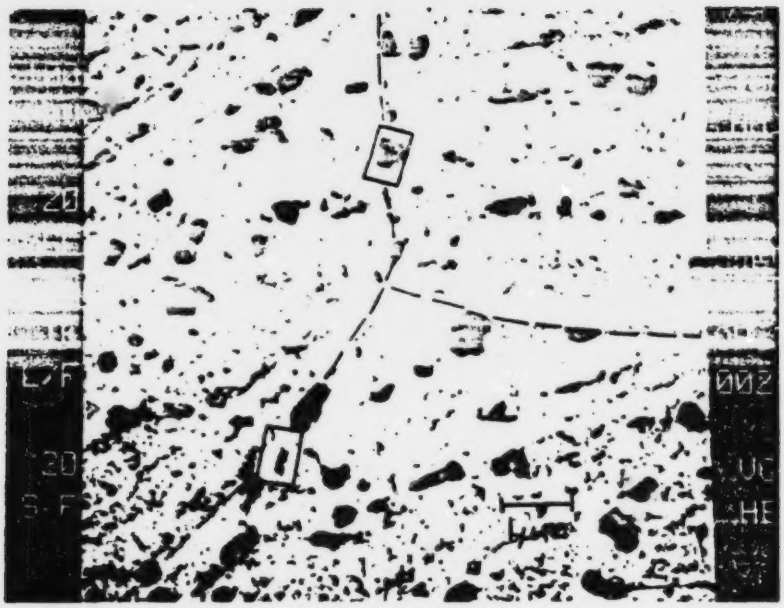

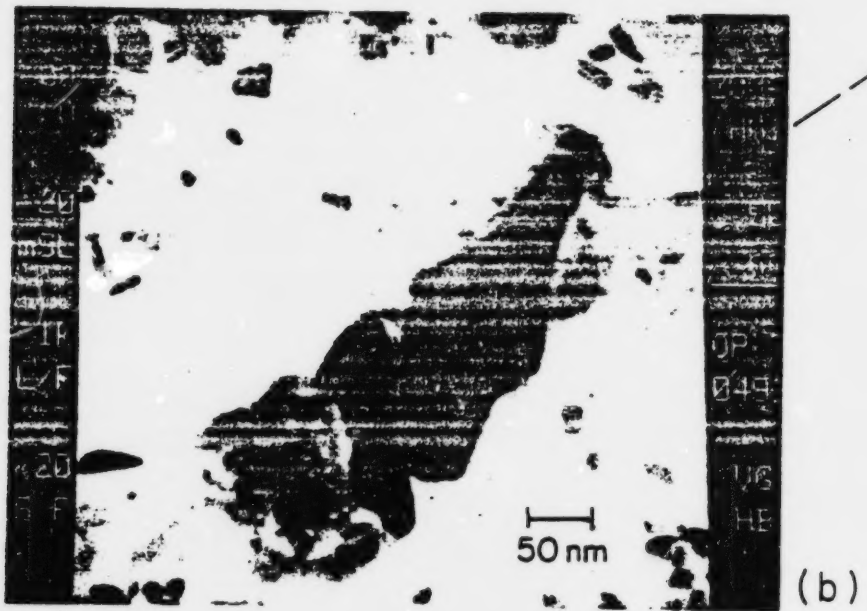

Fig. 6 Bright field images of type C and D carbides in P_2, after creep at 600°C, under 150 MPa, up to fracture, t_R = 777 hours. Type C carbides (b) are located in a prior austenitic grain-boundary as indicated above (in (a)).

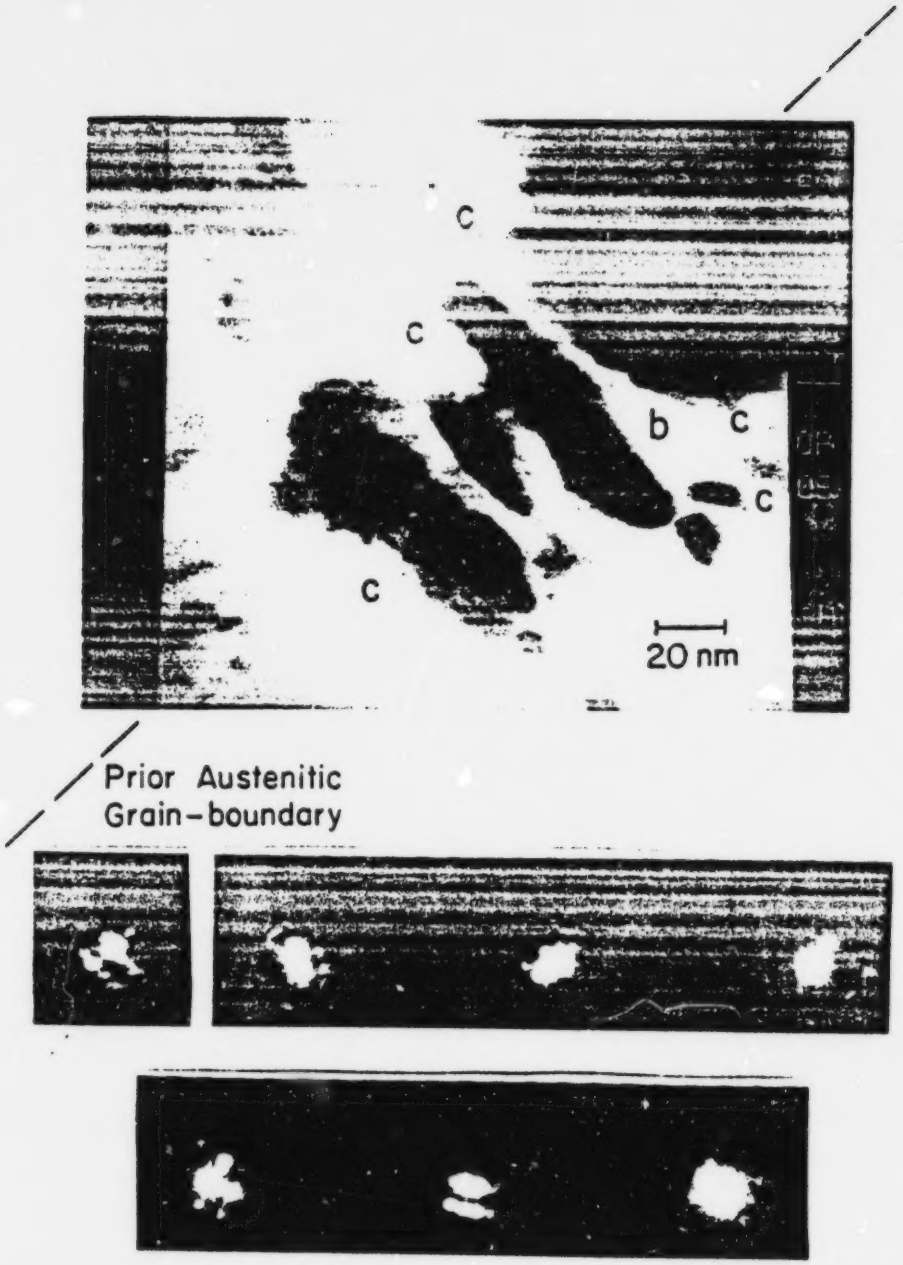

Fig. 7. Bright field image of type C carbides in a prior austenitic grain-boundary of P_2, after creep at 600°C under 150 MPa, up to fracture, t_R = 777 hours (location in the gb indicated in fig. 6a) Tilts from these carbides are compatible with the F.c.c. structure of M_2C.

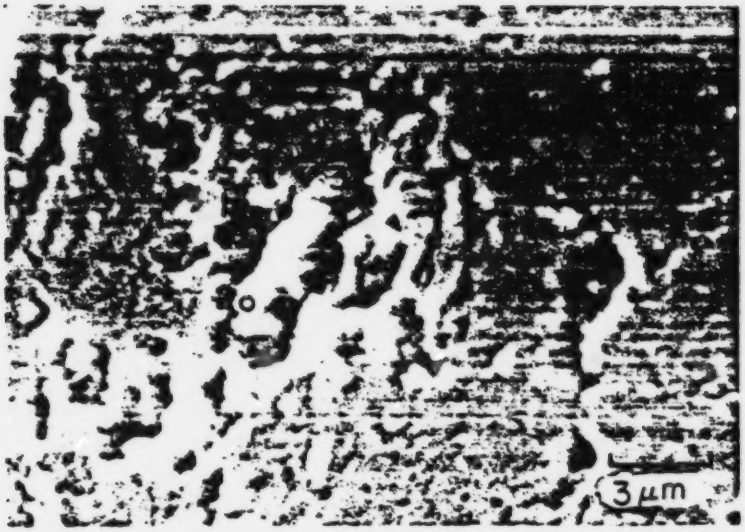

#	LOCATION	P conc. (at. %)
1	creep cavity	28.4
2	" "	30.0
3	" "	27.3
4	gb	21.8
5	"	22.6

Fig. 8. Creep cavities in the prior austenitic grain-boundaries of P_2, after creep at 600°C under 150 MPa, up to fracture, t_R = 777 hours.

Section B

Experience with Electron Energy Loss Spectrometry (EELS) on the VG HB5

(This work was performed by Dr. B. Robertson.)

It was initially hoped to use the EELS detector to measure C/N ratios in extracted particles from HSLA steels. However, the VG HB5 at McMaster had a series of major problems with the EELS unit including poor slit design, difficulty in interfacing with the KEVEX unit and a grounding problem in the spectrometer. Further, the collection efficiency of the system as designed at VG is low. Thus a sextripole lens was designed in order to increase the collection efficiency by an order of magnitude. The sextripole designed at McMaster was not initially successful due to changing of the annular dark field detector which deflected the beam entering the spectrometer. This problem has now been resolved.

However, to date the EELS system has not yielded useful analytical data in regard to light element analysis. It is also apparent that the EELS system is unlikely to operate as a self-consistent analytical system in which experimental spectra can be compared with calculations based on cross-section data. Thus in the future, if EELS is to be used as a system of analysis for light elements, a library of standards of known composition must be assembled and characterized for a variety of instruments including the VG HB5.

Section C

Replication Methods for Combined EELS and X-ray Analysis

(This section of the work was performed by Dr. V. Raghunathan.)

In preparing extraction replicas for EELS it is necessary to utilize support films which do not contain carbon. A technique for preparing SiO as a support film was previously described by Ritter, Hall and Denne, (Proc. of 4th E.M.S.A. Meeting, p. 502). A major difficulty with this technique is that thick films are opaque to the beam and thin films are too fragile to handle easily for microscopy.

In the present work two types of support film were developed, SiO and Al. It was found that standard metallographic preparation followed by etching with hydrogen peroxide and hydrofloric acid was the best method of preparing the sample surface. SiO was used in the form of pellets deposited on the sample using electron beam heating at a pressure of 10^{-6} torr or better. A range of film thicknesses from 20 - 80 nm were studied and it was found that the optimum thickness was of the order of 35 nm. It was found to be advantageous to use a film thickness gauge to monitor the thickness of the deposited films. The film thickness can also be estimated from the relative intensity of the zero loss and plasma loss peaks.

To produce the Al support films, Al was deposited from a resistance heater onto the etched surface of the metal using thicknesses of 70 - 120 nm.

The Al extraction replica does not appear to work well for the extraction of small particles but extracts the larger dendritic particles very efficiently.

Unlike carbon replicas both the Al and SiO replicas tend to deteriorate with storage.

Examples of SiO and Al replicas are shown on the following page.

a)

b)

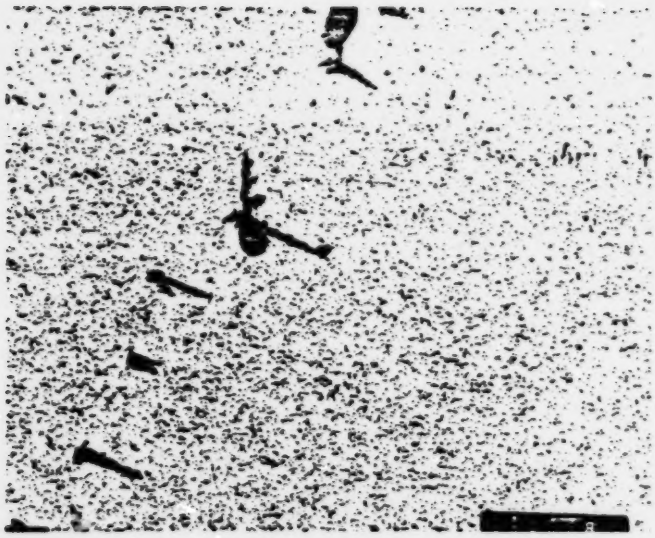

Figure 1 - a) and b) --Al extraction replica
c) and d) --SiO extraction replica

c)

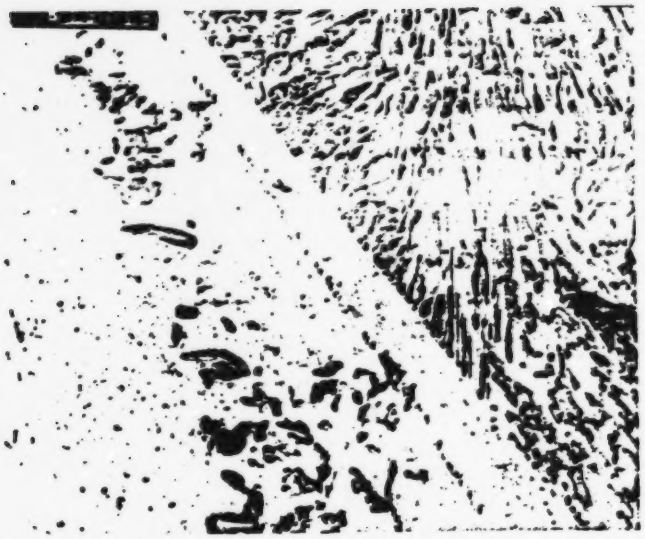

d)

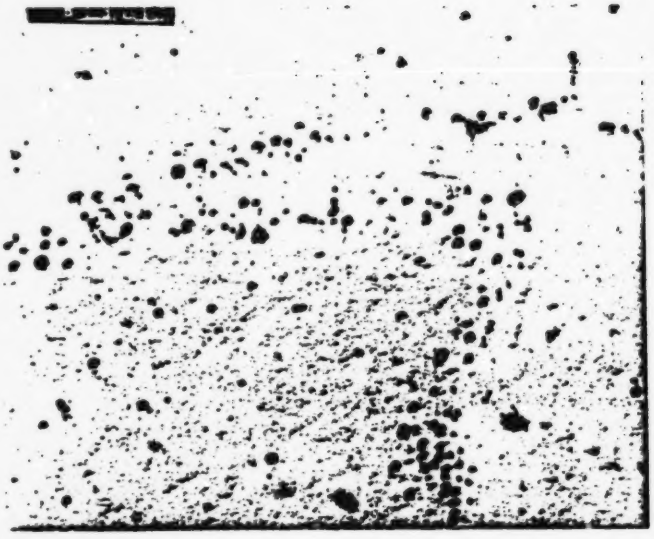

Section D

Observations of the Structure of Shear Bands

(This section of the report is based on work performed by Dr. V.S. Raghunathan and Dr. A. Korbel).

There have been a number of studies which indicate that at large strains deformation is often accomplished by the formation and growth of macroscopic shear bands which traverse the entire cross-section of polycrystals rather than the motion of dislocations within individual grains. A review of the basic macroscopic plasticity models relating to shear band formation has appeared in Scripta Metallurgica 1984, 18, p. 421-455. However, to date there is little experimental evidence available concerning the detailed structural characteristics of the shear bands.

Thus as part of an ongoing study of the nature of shear bands and their relationships to fracture processes a detailed TEM study was made of the nature of the shear bands occurring in polycrystals of Al-Mg-Zn and in single crystals of Cu-6%Al. The detailed accounts of these studies have been published elsewhere (viz. A. Korbel, V.S. Raghunathan, D. Teirlinck, W. Spitzig, O. Richmond and J.D. Embury, "A structural study of the influence of pressure on shear band formation", Acta. Met. 1984 32 511-519; J.D. Embury, A. Korbel, V.S. Raghunathan and J. Rys. "Shear Band Formation in Cold Rolled Cu-6%/Al Single Crystals", Acta. Met. 1984, in press). Thus in this report only the essential structural features are summarized.

In the work on Al-2%Mg-5%Zn tensile tests were conducted

under superimposed pressures varying from 0 to 1100 MPa. With increased hydrostatic pressure it was observed that there was no change in the strain required for the onset of shear bands, but that the ductility increased with increasing pressure due to the reduction in damage rate within the bands with increasing pressure.

In attempting to analyze the structure of shear bands which crossed several grains (as shown in fig. 1) it was found that in some regions the band consisted of simple shear events one slip system and in others it involved local utilization of a number of slip systems. These processes can be seen in figure 2 by comparing the selected area diffraction patterns obtained from shear bands in grains A and B. In grain A a simple diffraction pattern occurs and the local orientation of the shear band is crystallographic due to slip on the $(II\bar{I})$ plane. However, in grain B the shear band gives rise to a well developed spotty ring pattern. This is clear evidence for the operation of multiple slip systems as the diffraction pattern must reflect the occurrence of large misorientations in small regions of the grain. Thus in grain B the local orientation of the shear band is noncrystallographic in form. These observations indicate that the growth of shear bands across the cross-section of the sample involves a spatial distribution of regions of simple slip which are similar to coarse slip bands which are interspersed with narrow regions of localized multiple slip. Although, the constitutive shear processes involves crystallographic slip the overall macroscopic band can appear non crystallographic in form.

In fig. 3 another example of the interelation of the coarse slip (seen in the grain on the right in figure 3) and the multi slip region of the band (seen in the grain on the left) is shown. This micrograph shows two important features of the strain localization process. The sharp steps at the grain boundary indicate that offsets of the order of 1000 burgers vectors can be produced during shear band propagation which raises important questions as to the mechanism by which grain boundaries are penetrated.

The second feature of regions such as those shown in figure 3 is that it appears that within the shear band the small precipitates of η' are removed which may in this case be the structural softening process associated with strain localization. In contrast in Cu-6%Al single crystals the low stacking fault energy results in planar slip and hence the anlysis of the crystallography of local slip systems is made earlier.

Experiments were conducted on single crystals of Cu-6%Al with the rolling plane being either $(\bar{3}\bar{2}1)$ (designated OM) or $(1\bar{1}1)$ (designated OT).

Optical metallography indicated as shown in figure 4, that above 40% rolling reduction shear bands are a very common mode of deformation.

Transmission electron microscopy of crystals of both orientations revealed a number of important features of the shear bands. In many cases it is clear that the regions of intense shear are able to pass through the existing substructure (Fig. 5). This indicates that some form of local instability must arise in order for the existing substructure to collapse and

arise in order for the existing substructure to collapse and allow slip to spread over large distances in the highly work hardened structure.

In general the orientation of the shear bands is non crystallographic although they may occur at very specific angles to the rolling plane. Thus, the shear bands may be locally segmented as shown in figure 6.

Diffraction patterns taken adjacent to and far from a shear band figure 7 indicate the local lattice distortion which may accompany shear banding.

These results indicate that in order to form macroscopic shear bands of apparently irrational habit plane a series of cooperative shear events are needed which must be spatially correlated throughout the crystal. In local regions these correlated slip events may give rise to large local lattice curvatures. The diffraction capability of the STEM is clearly of value in analyzing in detail this important mode of deformation.

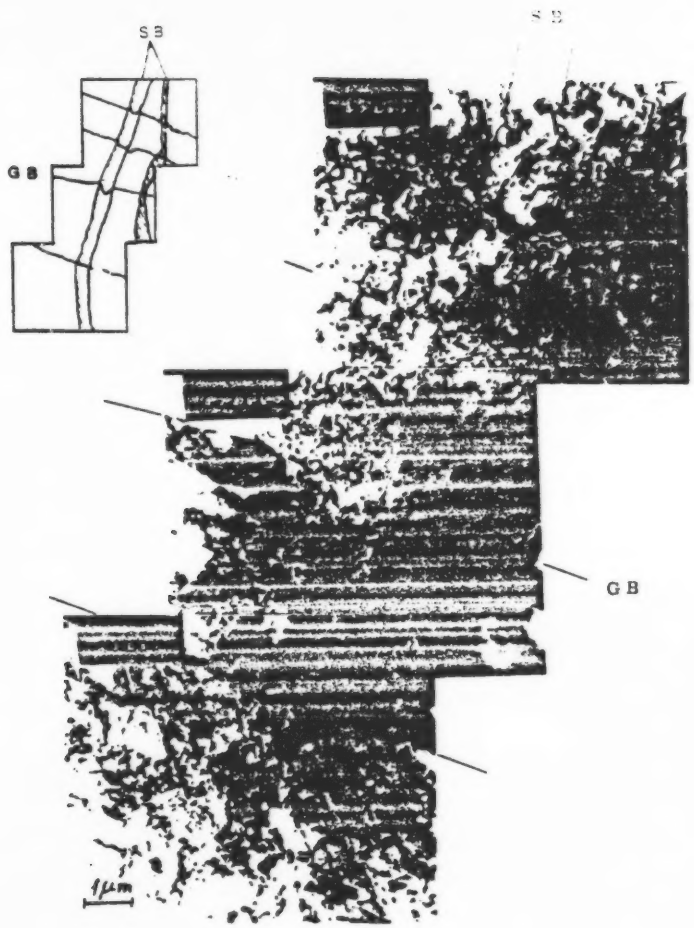

Fig. 1 - Montage of electron micrographs of the neck region of the sample tested in tension under a superimposed hydrostatic pressure of 1100MPa. Microscopic shear bands are crossing several grains. An accompanying sketch illustrates this.

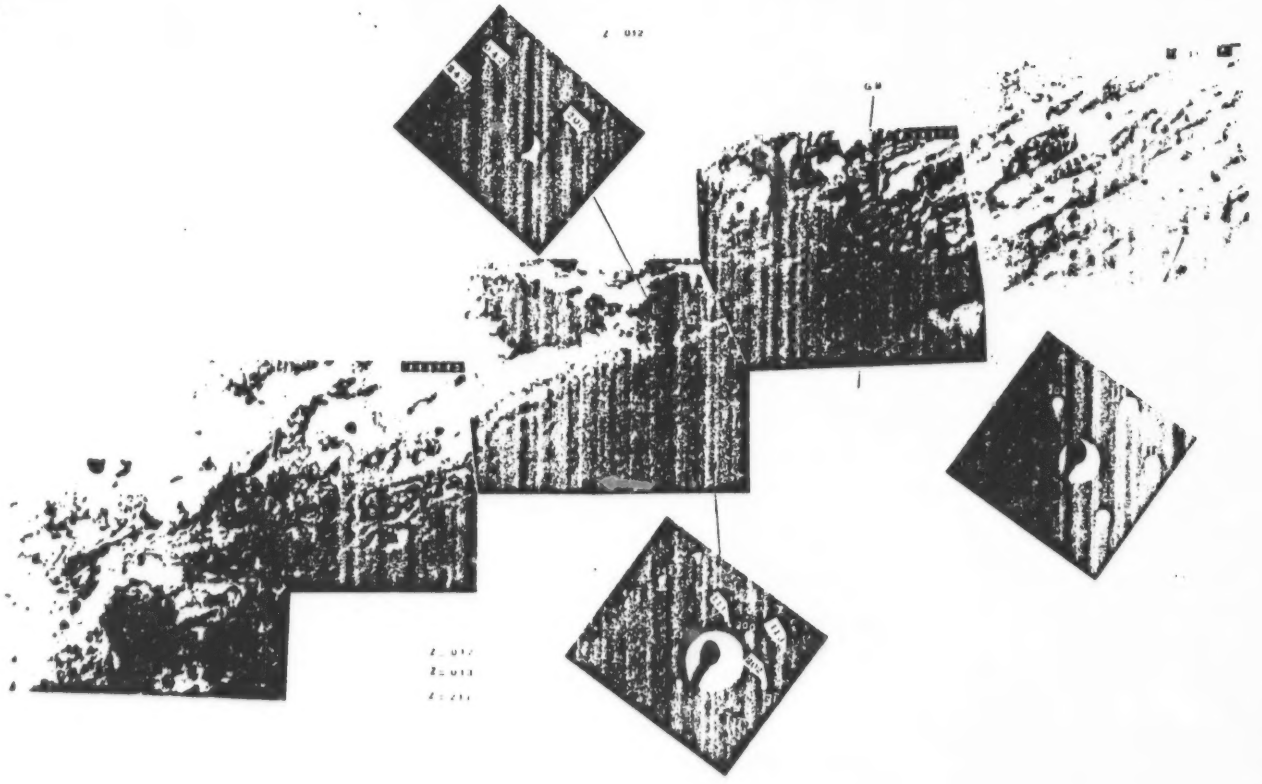

Fig. 2 - Montage of TEM micrographs from a coarse grained sample tested in plane strain tension under a superimposed hydrostatic pressure of 1100 MPa. The direction of shear band coincides with the crystallographic direction [325] which is the trace of the slip plane (111) on the foil in grain A.

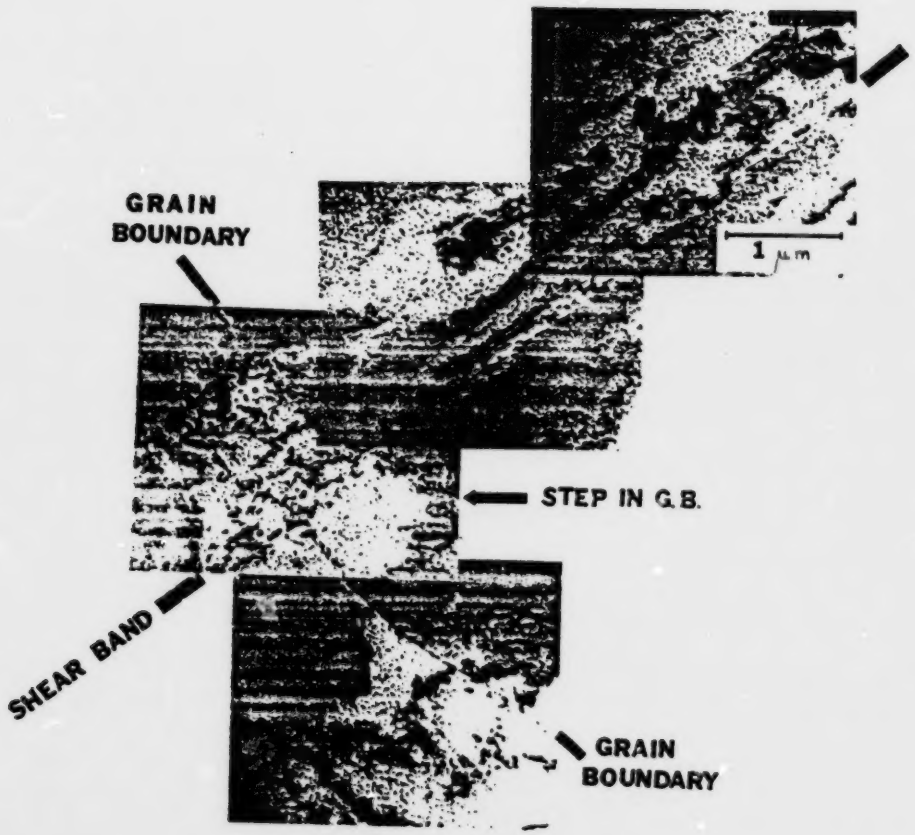

Fig. 3 - Montage of TEM micrograph of a sample tested in plane strain conditions under an imposed pressure of 1100 MPa, illustrating the change from coarse band to shear band mode of deformation.

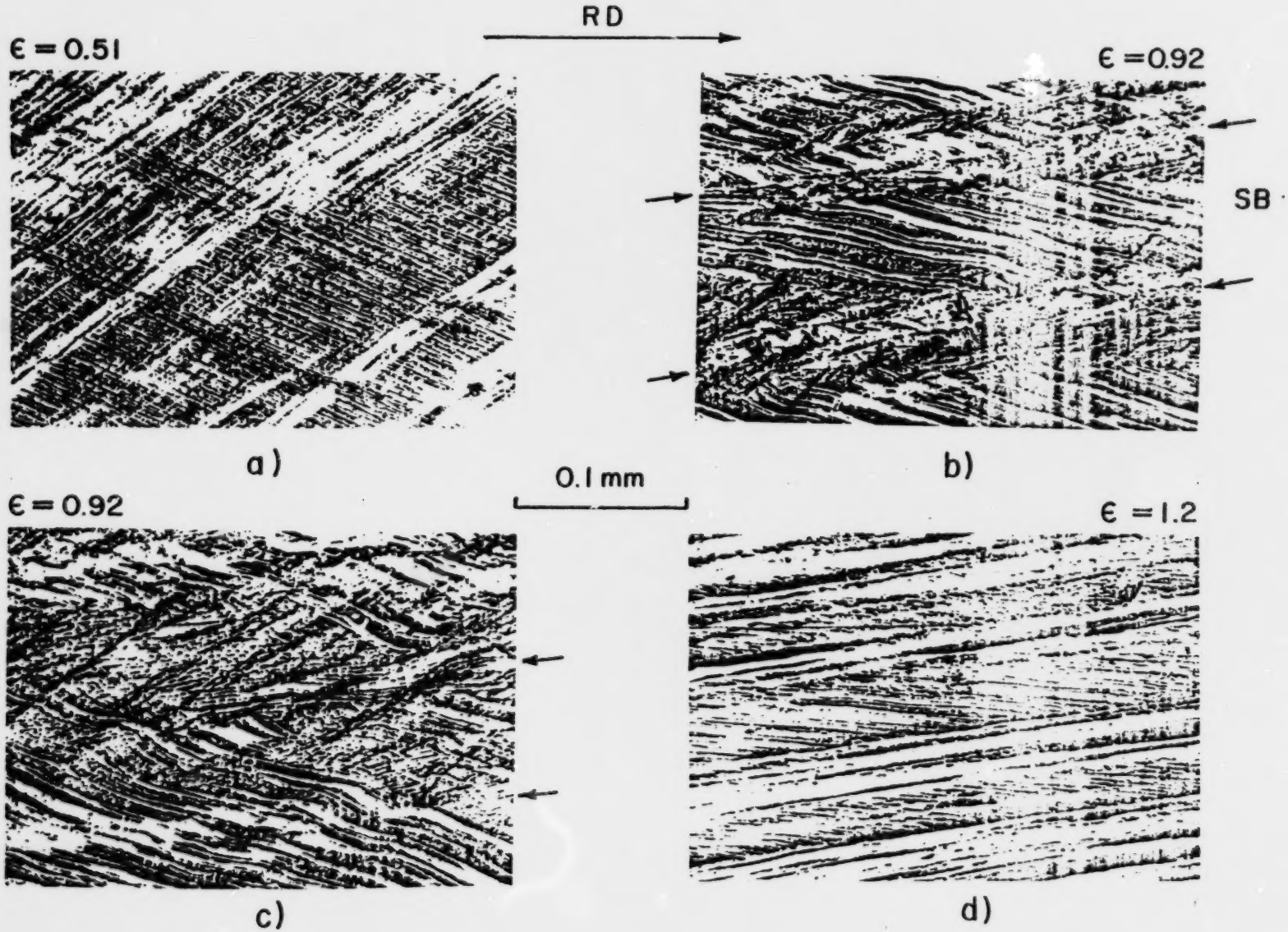

Fig. 4.- Optical micrographs of the structures observed in the longitudinal section of the 01 oriented crystal after different (a-d) rolling strains. Arrows indicates the shear bands.

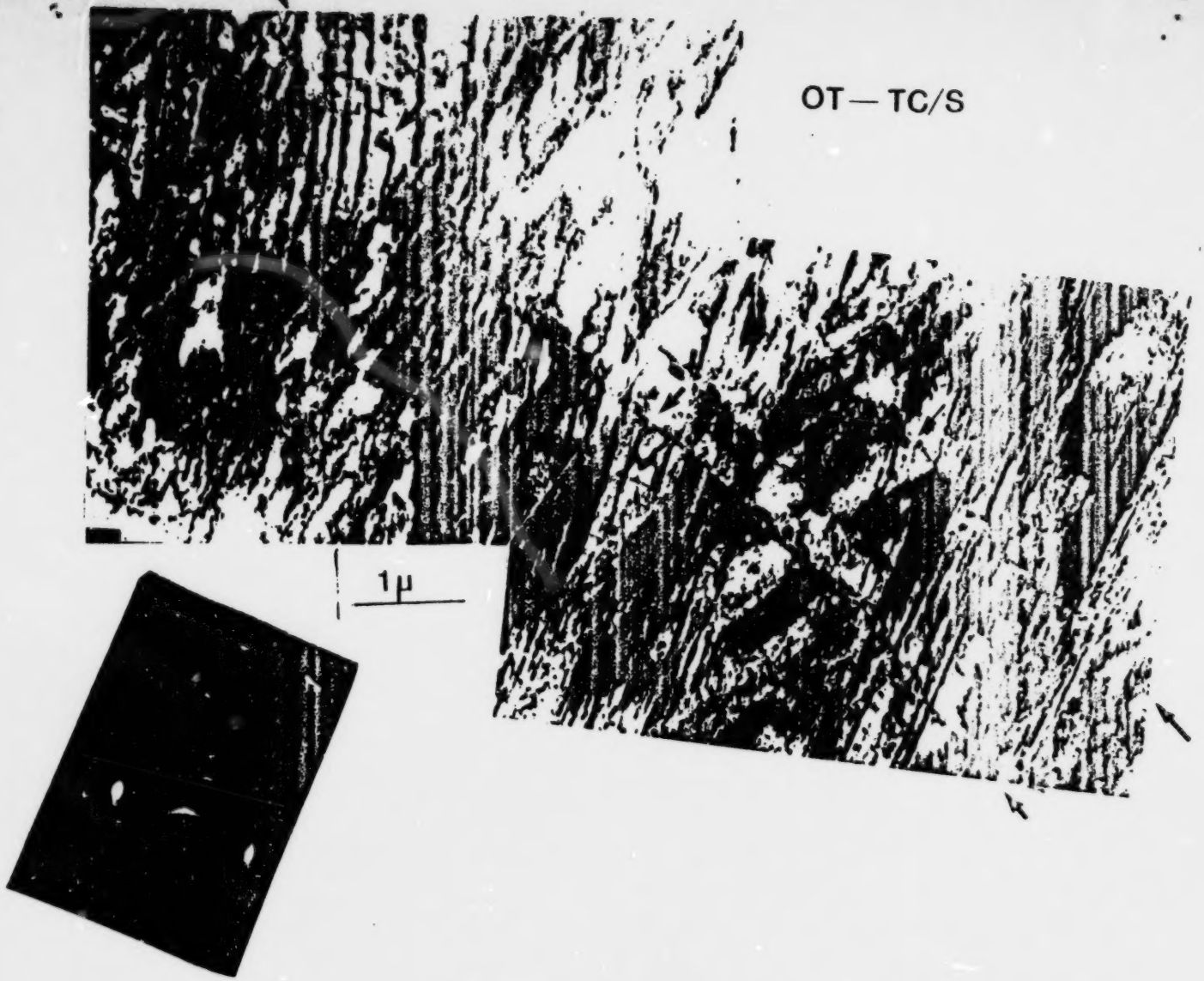

Fig. 5 - The structure observed in the transverse section of the OT crystal. Arrows indicate the layers of intense shear. (Note the scale asterism of diffraction spots).

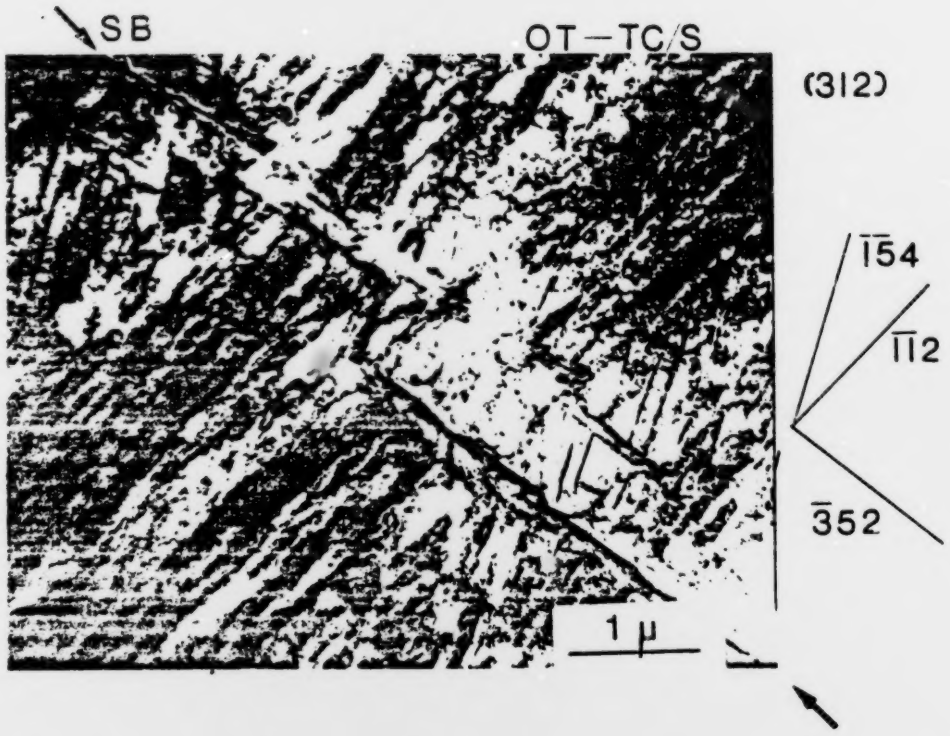

Fig. 6.- Multi-slip processes involved in band growth resulting in the segmented structure of the band and its overall non-crystallographic orientation.

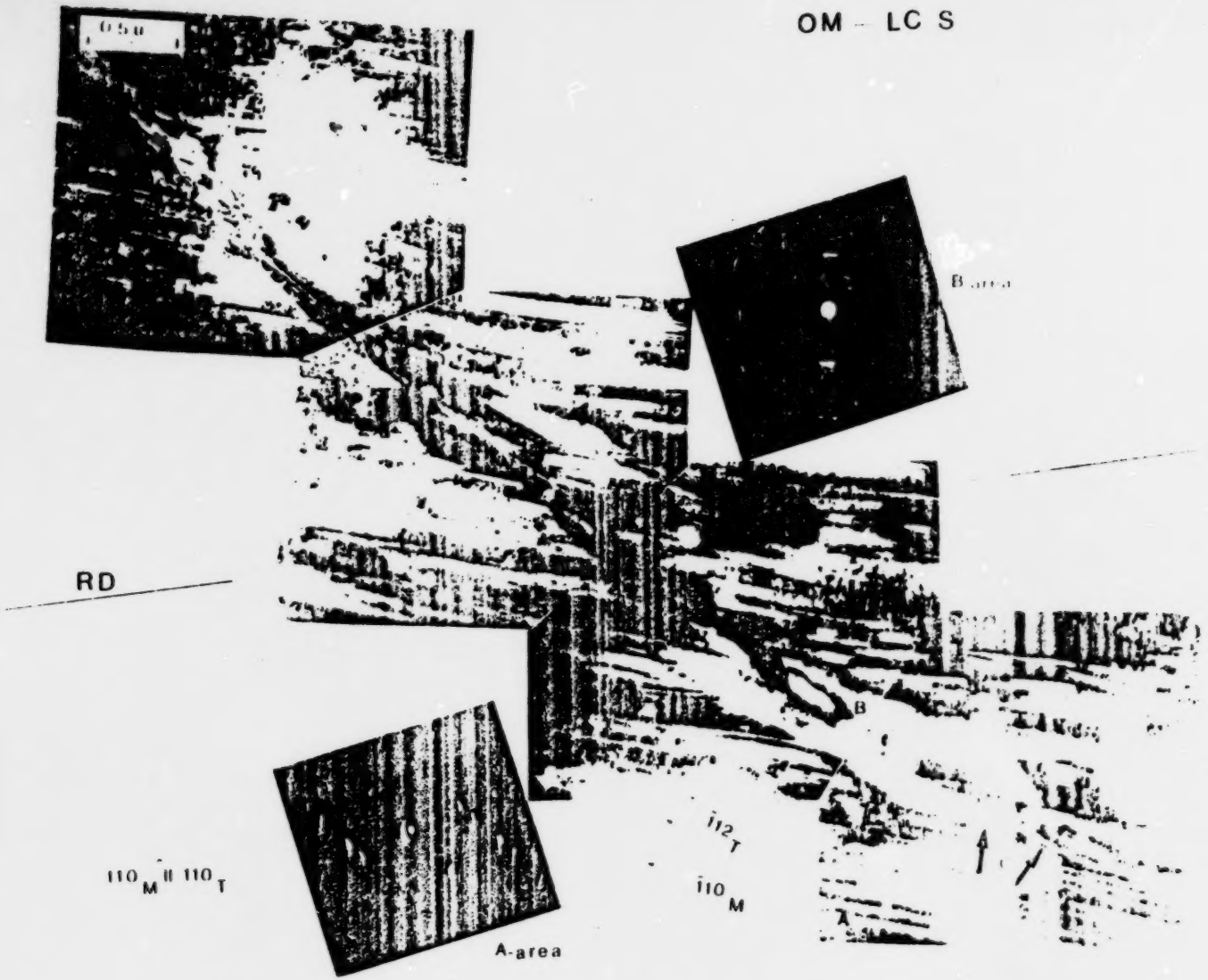

Fig. 7.- The structure observed in the LC/S of the OM oriented crystal showing shear band penetrating twins of the matrix. Distortion of the crystal lattice in the band is indicated by the asterism of diffraction spots.

Section E

Observations of the evolution of second phase particles in as cast H.S.L.A. steels.

(This section of the study was performed by Dr. V.S. Raghunathan, Mr. G. Ocampo and Mrs. Castillo and much of the theoretical interpretation was provided by Dr. Subramanian)

A detailed account of the experimental work related to this section of the report is contained in the Master's thesis written by Mr. G. Ocampo. Copies of this thesis have been submitted independently to CANMET. Thus, in this section only the salient features of the study will be considered.

In considering the phase transformation in as cast materials attention must be given to the scale of events occurring in dendritic growth during solidification relative to the size of second phase particles produced during the entire thermal history of the sample. In order to follow the evolution of the structure from the original δ dendrites through the subsequent $\delta \rightarrow \gamma$ and $\gamma \rightarrow \alpha$ transformations a series of etching and replication techniques were developed. These have been described in detail by Ocampo et al. Metallography 1983 and enable the location of the precipitates to be mapped in relation to the positions of the dendritic boundaries and other subsequent interfaces. An example of the mapping technique is shown in figure 1 which shows irregular shape particles decorating the initial as-cast boundaries. Detailed electron microscopy was performed on replicas taken from both the edge and centre regions of laboratory cast ingots of a variety of H.S.L.A. steels containing Nb and Ti. The composition of these steels is outlined in Table I.

The electron microscopy studies revealed two important features of the second phase particles. First a variety of particle morphologies were observed and some of these morphologies exhibited shape instabilities.

Examples of the various morphologies are shown in figures 2,3,4,5 and 6. The complex morphologies can arise in essentially two ways a) precipitation on prexisting interfaces and b) shape instabilities of simple cuboidal particles when they are subject to growth in a field of solute supersaturation summary of the various morphologies and compositions are given in Table II. The second important feature of the observations of the particles is their compositional inhomogeneity. Analysis in the STEM was able to reveal changes in the Ti/Nb ratio at various points in the particles as illustrated in figures 6 and 7. The compositional inhomogeneity is indicative to the occurrence of heterogeneous nucleation of one miroalloying phase on a pre-existing phase due to the structural similarities of the various carbides and nitrides. Due to lack of an adequate E.E.L.S. system it was not possible to determine the ratio of both Ti/Nb and N/C sequentially in the various particles. However one very puzzling aspect of the chemical inhomogeneity needs to be considered in detail. In some cases the centre region of the particles is rich in Ti. This is to be expected as TiN is the most stable phase which could occur and thus the sequence of nucleation would be expected to be the occurrence of TiN at high temperature and the subsequent heterogeneous nucleation of Nb rich phases at lower temperatures.

However, in other cases particles were observed which were rich in Nb at the centre and enriched in Ti at the outside. One possible explanation for this is that the phases involved are essentially carbides rather than nitrides. In this case the carbide of niobium is more stable and could occur at higher temperatures and hence serve as the substrate for heterogeneous nucleation of a titanium rich carbide. In the absence of a detailed E.E.L.S. analysis of the N/C ratios the above explanation must remain somewhat speculative.

It is clear from the observations described above that the second phase particles observed in the as-cast structures are both compositionally and spatially non-uniform. Thus, in order to discuss the possible sequence of precipitation involved the observed heterogeneous nucleation cognizance must be taken of the redistribution of solutes which occur both during solidification and in the subsequent cooling process. To date no complete analysis for this process exists in the literature. However, the classical analysis due to Scheil can be modified to consider diffusion occurring in the δ + liquid, δ , and γ phase fields down to about 1000 ^{o}C. This has been accomplished by Shima and Subramanian and applied to a variety of H.S.L.A. steels. The basic analysis predicts two important features: a) the profile of C and N across the dendrites are essentially uniform as shown in figure 8 and b) the Ti distribution is modified by the various stages in the cooling process as shown in figure 9. The resultant compositional profiles mean that in considering the

likely sequence of precipitates cognizance must be taken of the overall levels of Ti Nb N and C and the ratios which arise as a result of redistribution of the substitutional alloy elements.

TABLE I

Chemical Analyses of the Alloys

Alloy Designation	Element (wt %)									
	C	N	Ti	Nb	S	P	Si	Mn	Al	Mo
449	0.07	0.007	0.011	0.005	0.004	0.003	0.23	1.80	0.025	0.31
460	0.075	0.008	0.011	0.01	0.003	0.003	0.22	1.78	0.028	0.31
454	0.075	0.008	0.01	0.04	0.003	0.003	0.23	1.85	0.02	0.31
453	0.065	0.008	0.01	0.06	0.004	0.003	0.24	1.74	0.03	0.32

TABLE II

Details of Precipitates Analysis

Alloy Designation	Morphology of Precipitate	$\frac{C_{Ti}}{C_{Ti}+C_{Nb}}$ In alloy (Nom.w/o)	$\frac{C_{Ti}}{C_{Ti}+C_{Nb}}$ In precipitate (w/o) min-max.	Range Size nm	Location	Remarks
453 - Edge	Dendritic*	0.14	0.11 - 0.15	80-380	m,b	
	Cuboid		0.07 - 0.21	40-50	m	Few 400-2000 nm
	Angular		0.08 - 0.14	230-325	m	In rows
453 - Centre	Dendritic*		0.13 - 0.15	150-1950	m,b	
	Cuboid		0.08 - 0.21	40-50	m	
	Angular		0.07 - 0.23	200-700	m	In rows
454 - Edge	Dendritic*	0.2	0.12 - 0.24	60-970	m,b	
	Cuboid		0.09 - 0.33	25-40	m	
	Angular			130-390	m	Observed in TEM only; in rows
454 - Centre	Dendritic*		0.07 - 0.10	200-900	m	
	Cuboid		0.10 - 0.13	40-50	m,b	Few 300 nm
	Angular			250-900	m	Observed in TEM only; in rows

* More important morphology in the alloy

b = boundaries or sub-boundaries, m = matrix

TABLE II (Cont'd)

Alloy Designation	Morphology of Precipitate	$\frac{C_{Ti}}{C_{Ti}+C_{Nb}}$ In alloy (Nom.w/o)	$\frac{C_{Ti}}{C_{Ti}+C_{Nb}}$ In precipitate (w/o) min-max.	Range Size nm	Location	Remarks
460 - Edge	Dendritic	0.52	0.26 - 0.38	60-280	m	
	Angular*		0.21 - 0.52	110-325	m,b	In rows
460 - Centre	Dendritic*		0.15 - 0.32	85-420	m	
	Angular		0.32 - 0.47	60-140	m	In rows
	Spiked		0.29 - 0.52	160-220	m	
449 - Edge	Cuboid*	0.69	1.0 - 1.0	30-50	m	
449 - Centre	Cuboid		0.91 - 0.95	30-50	m	
	Spiked*		0.89 - 0.93	80-220	m	

* More important morphology in the alloy

b = boundaries or sub-boundaries, m = matrix

Figure 1 .- Composite micrograph of a carbon extraction replica, showing the decoration of primary grain boundaries by precipitates of irregular shape. (Alloy 454-Centre).

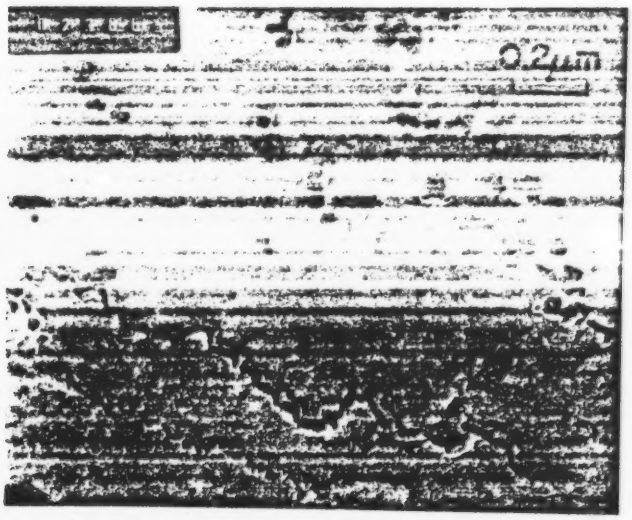

Figure 2 .- Typical angular precipitate in alloy 453 - Edge (TEM: carbon extraction replica).

Figure 3 .- Typical irregular precipitate on primary grain boundaries in allo 454 - Centre (TEM: carbon extraction replica)

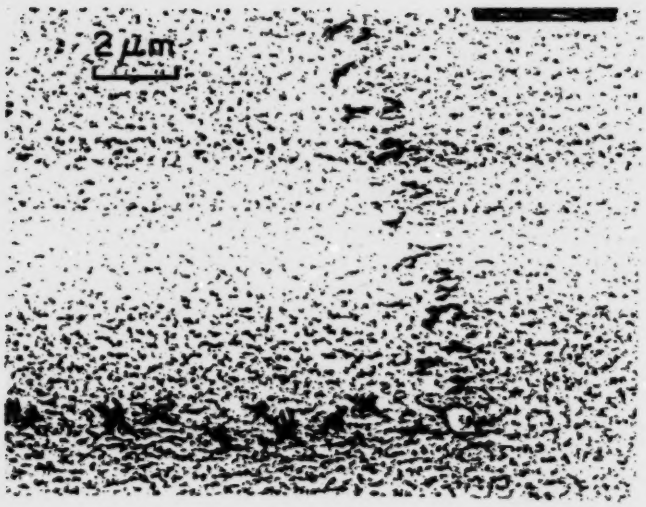

Figure 4.- Typical dendritic precipitate in alloy 453 - Centre. (TEM: carbon extraction replica).

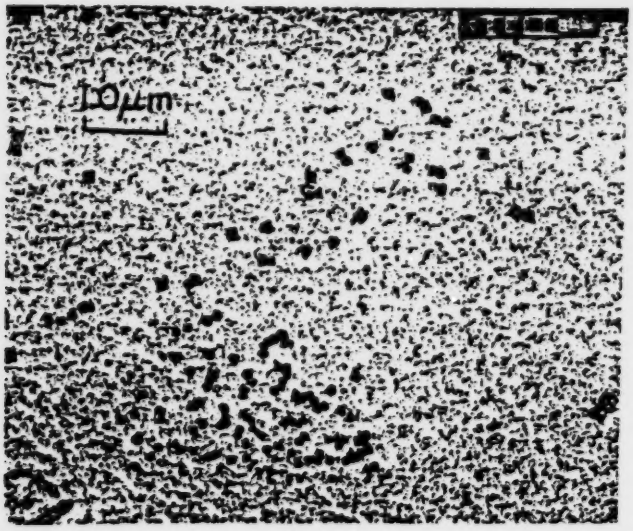

Figure 5.- Typical geometric or cuboidal precipitate in alloy 453 - Centre (TEM: carbon extraction replica).

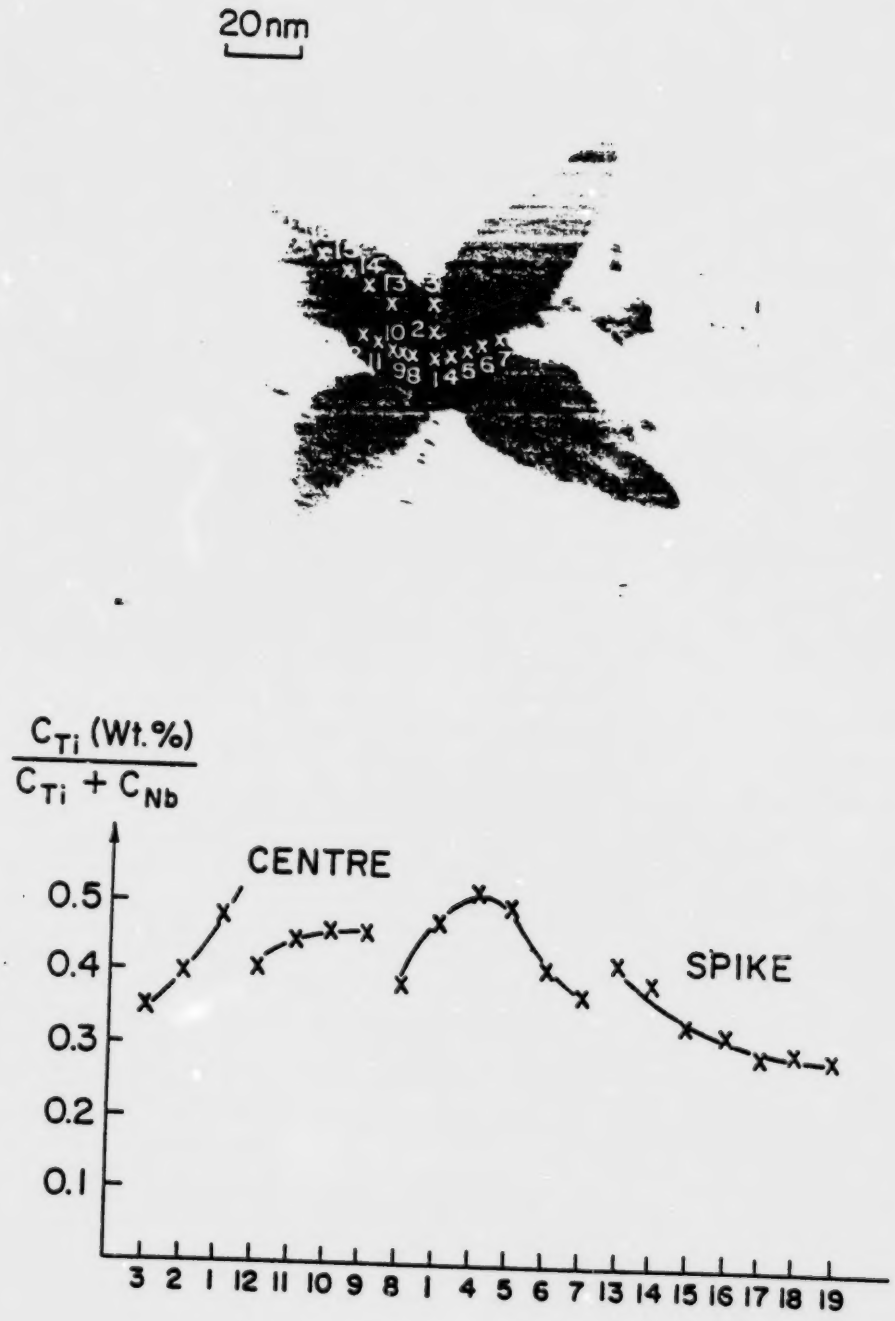

Figure 6: STEM microanalysis of a spiked precipitate. Central portion is rich in Ti, whereas Nb is enriched along the spikes. Protrusions are evident on spikes (Alloy 460 - Centre).

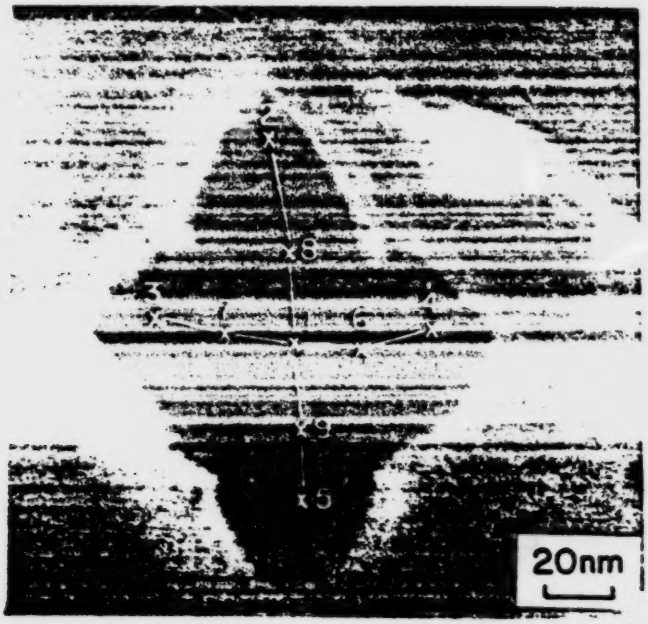

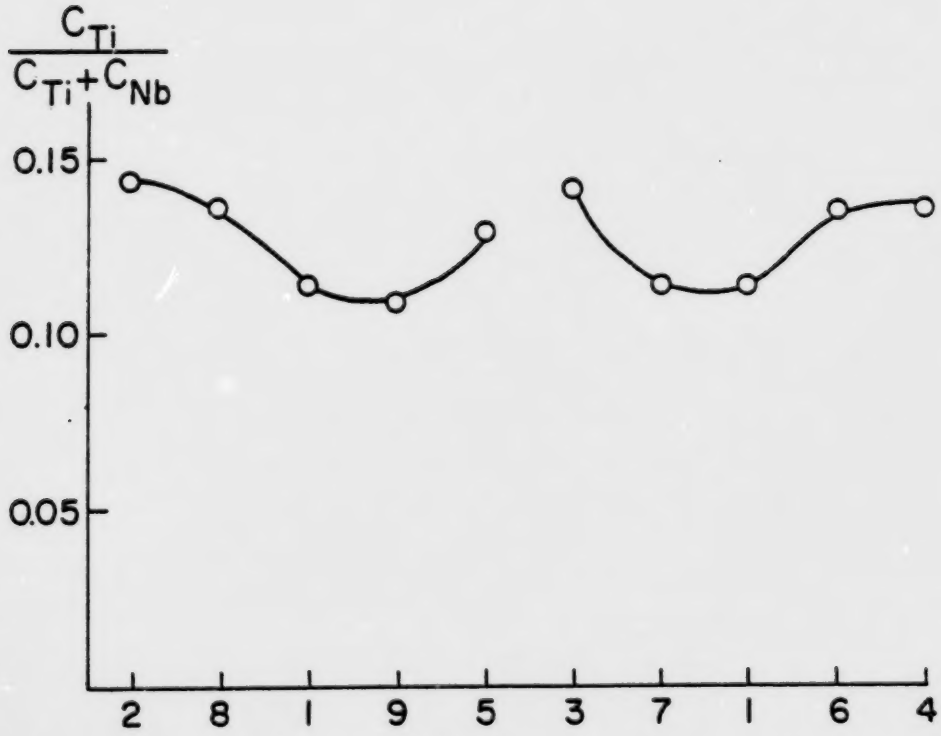

Figure 7 : Typical STEM microanalysis of a dendritic precipitate. Centre is rich in Nb (Alloy 453 - Edge).

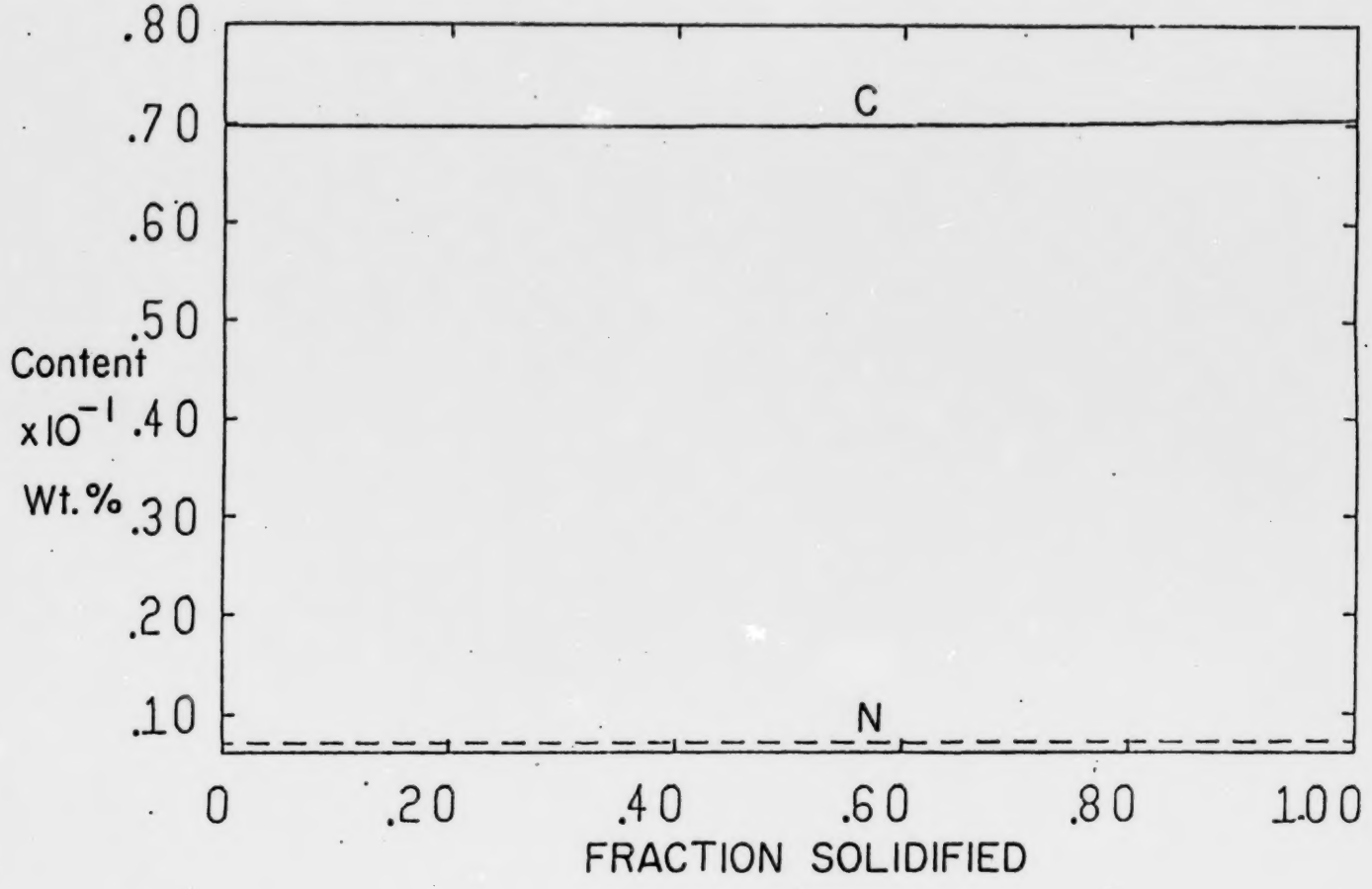

FIGURE 8.- C, N CONCENTRATION PROFILE AT THE END OF SOLIDIFICATION IN ALLOY 449.

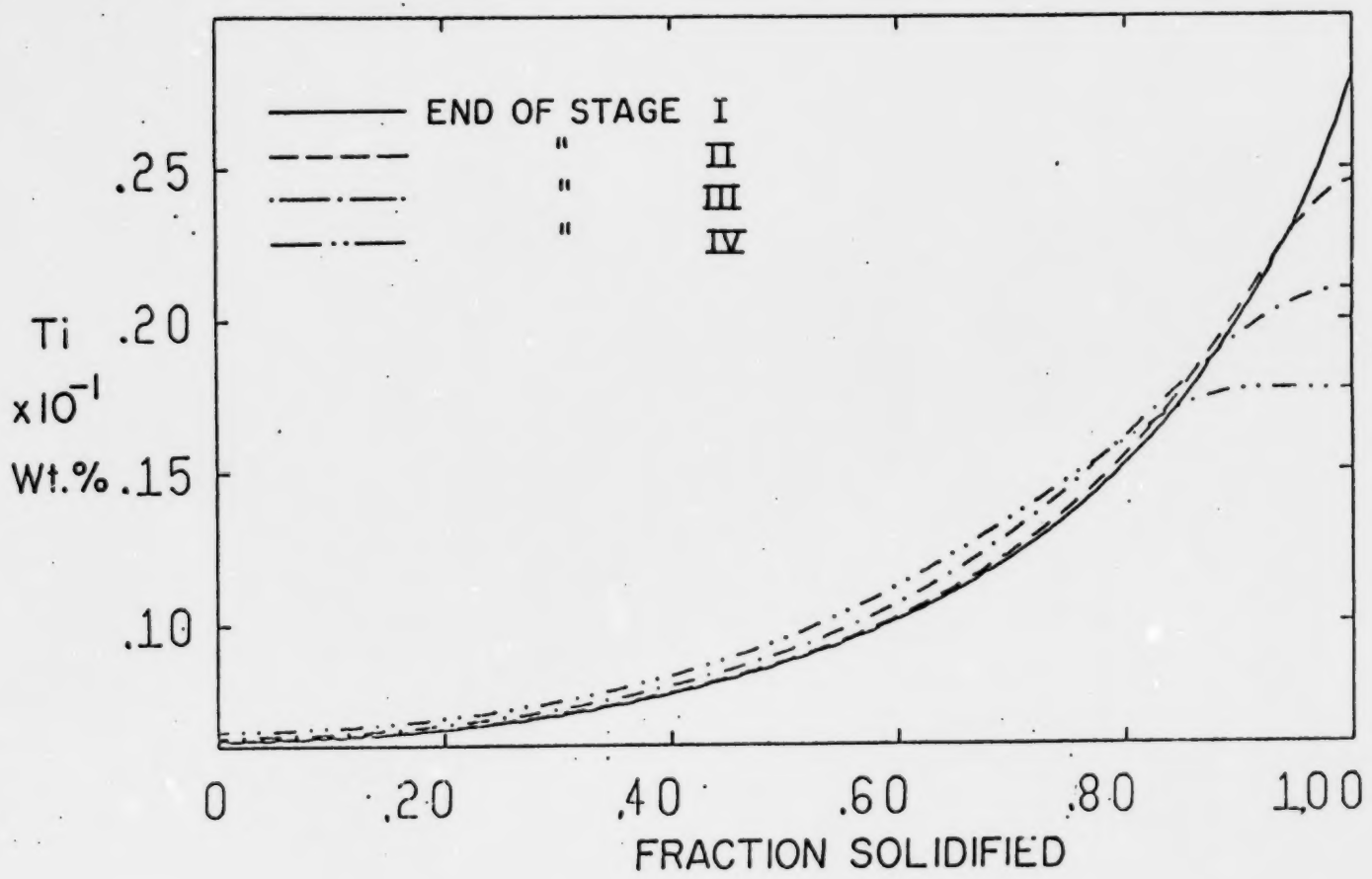

FIGURE 9.- DENDRITIC MICROSEGRATION OF Ti IN ALLOY 449.

Conclusions

The overall objective of the study was to delineate the value of scanning transmission electron microscopy to a range of current problems in physical metallurgy. The foregoing results clearly indicate both the problems and potential of STEM analysis. To date the H.B. 5 at McMaster has not proven to be capable of doing reproducible electron energy loss analysis and thus its applicability to a range of compositional analysis problem dealing with light elements is severely limited. It is hoped that this situation may be modified in the future or that the high spatial resolution of the HB5 could be combined with studies of E.E.L.S. performed on other instruments.

Another feature of the STEM analysis to be considered is the need to develop both replication techniques and standards to aid in the quantitative compositional analysis of second phase particles. This is essential for both the x-ray analysis of heavy elements and the E.E.L.S. analysis for light elements.

Let us now consider the advantages of the STEM in terms of its high spatial resolution. The work described in Section D clearly indicates that for many systems at large strains the mode of plastic deformation may change such that it is dominated by macroscopic shear band formation. The micro-diffraction capability of the STEM is clearly of value in analyzing both the lattice rotations accomplished in the shear band relative to the matrix and the strain gradients associated with the accomodation of shear bands. This latter capability is of enormous potential value to a range of problems including the analysis of the gradients which give rise to recrystallization in duplex

structures and the detailed events which occur in the transmission of plastic flow at grain boundaries.

The detailed compositional analysis described in Section E indicates the inherently new information available from the STEM in the area of phase transformations. The ability to measure compositional gradients with small second phase particles opens up new areas of study in regard to the occurrence of heterogeneous nucleation in solid state phase transformations and to the quantitative analysis of morphological instabilities in a wide range of systems. However, the brief review of the analysis of the data presented in Section E also indicates that in principle cognizance can be taken of the evolution of precipitate structures from the process of solidification through a range of solid state transformations in at least a semi-quantitative manner.

This type of study may be the precursor to a more direct utilization of analytical electron microscopy to the optimization of composition and processing of materials such as high quality structural steels. Thus it can be stated that although the STEM is not fully developed as an analytical technique its spatial resolution permits it to yield new data for a range of phenomena in physical metallurgy. Further the data can be allied with other techniques such as Auger analysis and other surface techniques plus a range of metallographic methods which yield data on a coarser scale to give a more quantitative and comprehensive description of a number of phenomena of direct technological importance in the steel industry.

Acknowledgements

This work was performed for the Physical Metallurgy Research Laboratories, Energy, Mines and Resources Canada under Supply and Services Contract No. OSU81-00230. The authors are grateful to PMRL - CANMET for the provision of experimental materials and permission to publish this work. The authors acknowledge the support of Drs.J.D.Boyd and T.Malis in the scientific administration of the contract, along with many useful discussions concerning the direction and outcome of the experimental work.